The Spc105^{Knl1}/Kre28^{Zwint} complex promotes mitotic error correction by outer kinetochore recruitment of the Ipl1$^{Aurora\ B}$ kinase

Alexander Dudziak[1], Jasmin Schmidt[1], Frederik Hamm[1], Sharvari Tendulkar[1], Karolin Jänen[1], Ingrid R. Vetter[2], Sylvia Singh[3], Josef Fischböck[3], Franz Herzog[3,4] and Stefan Westermann[1]

[1]Department of Molecular Genetics I, Faculty of Biology, Center of Medical Biotechnology, University of Duisburg-Essen, Universitätsstrasse 5, 45117 Essen, Germany

[2]Department of Mechanistic Cell Biology, Max-Planck-Institute of Molecular Physiology, Otto-Hahn-Straße 11, 44227 Dortmund, Germany

[3]Gene Center Munich and Department of Biochemistry, Ludwig-Maximilians-Universität München, Feodor-Lynen-Str. 25, 81377 Munich, Germany

[4]Institute Krems Bioanalytics, IMC University of Applied Sciences, Krems, Piaristengasse 1, A-3500 Krems, Austria

[#]correspondence to: Stefan.Westermann@uni-due.de

Characters: 42,871 (no spaces, excluding Materials/Methods and References)

Keywords: chromosome biorientation, error correction, Aurora B, chromosomal passenger complex

Subject Categories: Cell Cycle, Biochemistry, Genetics

Working title: Outer kinetochore receptor of Ipl1$^{Aurora\ B}$ during error correction

Abstract

Kinetochores link chromosomes to dynamic microtubules of the mitotic spindle. To ensure equal chromosome segregation, sister chromatids must attach to microtubules from opposing spindle poles, a configuration referred to as biorientation. To avoid chromosome missegregation the conserved kinase Aurora B phosphorylates outer kinetochore proteins on attachments lacking tension, allowing re-establishment of new connections until biorientation is achieved. While Aurora B localizes to the centromere and inner kinetochore as part of the chromosomal passenger complex (CPC), the underlying recruitment pathways can be eliminated without fully disrupting biorientation. It therefore remains unclear how the kinase operates during error correction and whether additional mechanisms may facilitate tension-dependent phosphorylation of substrate proteins.

In this study, we identify the conserved KMN subcomplex Spc105^{Knl1}/Kre28^{Zwint} as an outer kinetochore receptor of the Aurora kinase Ipl1 in *Saccharomyces cerevisiae*. We show that mutations in the helical bundle domain of Spc105/Kre28 cause defective mitotic error correction, closely resembling the effects of *ipl1* or *sli15* mutants. In biochemical experiments we show that Ipl1/Sli15 directly associates with the KMN network via the Spc105/Kre28 subcomplex and that binding is inhibited by Ipl1 autophosphorylation. The phenotype of the *kre28* mutant cells can be efficiently suppressed by artificial recruitment of Ipl1, demonstrating the importance of Ipl1 docking to the outer kinetochore. These results have important implications for the mechanism of tension-dependent error correction during chromosome biorientation.

Introduction

Faithful chromosome segregation during mitosis depends on the physical interaction between highly dynamic microtubules of the mitotic spindle and kinetochores which assemble on centromeric DNA of each sister chromatid. Kinetochores are megadalton-sized proteinaceous structures consisting of multiple subcomplexes which fulfill different functions and assemble in a hierarchical manner. The constitutive centromere-associated network (CCAN) is the main constituent of the inner kinetochore[1-3] which is recruited to centromeres through the interaction of the Mif2^{CENP-C} subunit with centromeric nucleosomes[4,5]. The CCAN consecutively recruits subcomplexes of the outer kinetochore generally termed as KMN network which consists of the Spc105^{Knl1}/Kre28^{Zwint} complex, Mtw1 complex (Mtw1, Dsn1, Nnf1, Nsl1) and Ndc80 complex (Ndc80, Nuf2, Spc24, Spc25)[6,7]. In this context, the Mtw1 complex serves as scaffold which connects the other KMN subcomplexes with the inner kinetochore by direct association with Mif2^{CENP-C} and Ame1^{CENP-U} [8-12]. The highly elongated Ndc80 complex is the main microtubule receptor of the kinetochore which binds to the mitotic spindle through the calponin homology (CH) domains at the N-termini of the Ndc80 and Nuf2 subunits[13-15]. The Ndc80/Nuf2 head also recruits the checkpoint kinase Mps1 to the kinetochore[16-18]. The RWD domains of the Spc24 and Spc25 subunits connect the Ndc80 complex with the Mtw1 complex[8,10,19]. Furthermore, the Mtw1 complex recruits Spc105^{Knl1}/Kre28^{Zwint} to the kinetochore, even though the molecular mechanisms differ between mammals and yeast[20-22]. It has been well established that Spc105^{Knl1} plays a crucial role as a signaling platform for the spindle assembly checkpoint (SAC) after phosphorylation of MELT repeats by the conserved kinase Mps1[23-25]. Furthermore, Spc105^{Knl1} is required for recruitment of different protein phosphatases which are involved in SAC silencing and modulation of kinetochore-microtubule attachments[26-28]. In contrast, relatively little is known about Kre28^{Zwint} (also referred to as YDR532C according to its systematic name). Kre28 was identified as budding yeast homolog of the metazoan protein Zwint (Zeste White interacting protein) due its sequence similarity and, similar to Zwint, Kre28 forms a complex with Spc105^{Knl1} [29]. In contrast to mammalian cells, where the tandem RWD domains of Knl1 directly associate with the Mtw1 complex[20], *S. cerevisiae* Kre28 itself binds to the Mtw1 complex and by this recruits Spc105^{Knl1} to the kinetochore[21,22]. Both, the interaction with Spc105^{Knl1} and with the Mtw1 complex is mediated by coiled-coil elements in the central region of Kre28[21,22]. Furthermore, the C-terminus of Kre28 (residues 299-386) forms an RWD domain whose function is unknown so far[30]. Kre28 is essential for viability of yeast cells[29]. However, it is unclear whether this is just a consequence of loss of Spc105^{Knl1} from kinetochores or whether Kre28^{Zwint} has additional essential functions. For instance, it was proposed that Spc105^{Knl1}/Kre28^{Zwint} might be required for kinetochore localization of different microtubule-associated proteins[29].

The conserved protein kinase Ipl1$^{Aurora\ B}$ is an essential part of the error correction machinery

which phosphorylates outer kinetochore substrates in order to release kinetochore-microtubule attachments that lack tension[31]. Ipl1$^{Aurora\ B}$ acts in a complex with Sli15^{INCENP}, Bir1^{Survivin} and Nbl1^{Borealin}, together termed as chromosomal passenger complex (CPC). The N-terminal CEN box of Sli15^{INCENP} associates with Bir1^{Survivin} and Nbl1^{Borealin} [32] whereas its C-terminal IN box binds to the kinase domain of Ipl1$^{Aurora\ B}$ [33]. The CPC is targeted to the inner and kinetochore-proximal centromere by different mechanisms which depend on the haspin kinase, the Bub1 kinase and Sgo1/Sgo2[34]. However, different studies have demonstrated that inner and kinetochore-proximal centromere localization of Ipl1$^{Aurora\ B}$ is dispensable for establishment of biorientation. For instance, an N-terminal deletion of Sli15, preventing inner centromere recruitment of the CPC through Bir1, still supports the formation of bioriented attachments[35], suggesting that additional mechanisms can target the CPC to the kinetochore. Indeed, two recent studies identified the inner kinetochore COMA complex as a Bir1-independent Ipl1/Sli15 receptor[36,37]. Furthermore, studies in human cells have also suggested the existence of an additional pool of Aurora B at the kinetochore, which might be relevant for the phosphorylation of outer kinetochore proteins such as components of the KMN network[38,39].

In this study, we provide a detailed molecular analysis of the KMN subunit Kre28^{Zwint}. We identified a conserved Zwint helix in Kre28 whose lack leads to fatal chromosome segregation defects when cells are forced to reform their spindle apparatus after nocodazole washout. Artificial recruitment of Ipl1 to the outer kinetochore is sufficient to suppress this phenotype. Using protein biochemistry, we demonstrate that Spc105^{Knl1}/Kre28^{Zwint} can directly recruit Ipl1$^{Aurora\ B}$/Sli15^{INCEP} *in vitro* and that this interaction is negatively regulated by Ipl1 autophosphorylation. Thus, we have identified Spc105/Kre28 as the elusive outer kinetochore receptor of Ipl1 and we propose a model for how docking of the kinase may contribute to tension-sensitive mitotic error correction.

Results

Characterization of novel mutant alleles in the outer kinetochore subunit Kre28^{Zwint}

To gain insight into the organization of Spc105/Kre28 we performed AF2 structure predictions using the C-terminal part of Spc105 (omitting the disordered residues 1-489) and full-length Kre28 (**Figure 1 A, Figure 1 – Supplement 1**). The model shows that the Spc105/Kre28 heterodimer is formed via two interfaces: At the C-terminus of Kre28 a single RWD domain (residues 299-385) is paired with the N-RWD domain of Spc105. Together with short alpha-helical segments just preceding these RWD domains, this part resembles heterodimeric RWD domain arrangements found in other kinetochore subunits like Spc24/Spc25[40]. The N-terminal parts, on the other hand, engage into a helical bundle (**Figure 1 A**). This is in agreement with previous studies that have established that Kre28 associates with Spc105 mainly via coiled-coil segments formed by residues 127-201[22], while another segment (229-259) is required for binding to the Mtw1 complex[21]. Deletion of these segments is incompatible with KMN assembly and yields lethal phenotypes in yeast. Interestingly, multiple sequence alignments show that an alpha-helical segment preceding the first Kre28 coiled-coil domain (residues 77-113, hereafter referred to as the Zwint helix) is among the most conserved segments of the protein (**Figure 1 B**). By contrast, the C-terminus is not well conserved and human Zwint, for example, lacks an RWD domain[30].

To analyze the contribution of Zwint helix and RWD domain to Kre28 function in cells, we replaced the endogenous *KRE28* gene with Flag-tagged wildtype or mutant alleles in diploid cells (**Figure 1 C**). Tetrad dissection showed that neither *kre28*$^{\Delta Zwint}$ nor *kre28*$^{\Delta RWD}$ alone impaired viability. However, haploid spores of the *kre28*$^{\Delta Zwint\ \Delta RWD}$ double mutant were never recovered, demonstrating that simultaneous elimination of these segments is lethal (**Figure 1 C)**. Western blotting confirmed that wildtype and mutant proteins were expressed at comparable levels (**Figure 1 D**). Interestingly, serial dilution assays of the haploid strains revealed that *kre28*$^{\Delta Zwint}$ mutants fully supported growth at 30 °C, but were inviable in the presence of the microtubule-depolymerizing drug benomyl and additionally displayed cold sensitivity **(Figure 1 E**). By contrast the deletion of the C-terminal RWD domain of Kre28 did not cause a growth phenotype. We found that not only the complete removal of the Zwint helix, but also selected smaller deletions or point mutations of conserved residues caused benomyl hypersensitivity. The most pronounced phenotypes were obtained for truncations eliminating Kre28 residues 103-113, as well as for point mutations in this region (**Figure 1 – Supplement 2**).

149 **The *kre28$^{\Delta Zwint}$* mutant is defective in mitotic error correction of kinetochore-microtubule**
150 **attachments**

151 The pronounced benomyl hypersensitivity of the *kre28$^{\Delta Zwint}$* mutant may be caused by a defect
152 in the spindle assembly checkpoint (SAC) or a different problem with chromosome
153 segregation. To distinguish between these possibilities, we analyzed Pds1^{Securin} levels in
154 wildtype and *kre28$^{\Delta Zwint}$* strains after cells were released from a G1 arrest into medium
155 containing the microtubule-depolymerizing drug nocodazole. Both, wildtype and *kre28$^{\Delta Zwint}$*
156 mutant cells stabilized Pds1 levels, while a *mad1Δ* control strain failed to do so (**Figure 2 A**).
157 Thus, *kre28$^{\Delta Zwint}$* cells have a functional SAC response to a lack of kinetochore-microtubule
158 attachments. To define the genetic relationship between the *kre28$^{\Delta Zwint}$* mutant and the mitotic
159 checkpoint more closely, we deleted the *MAD1* gene in the *KRE28* wildtype or *kre28$^{\Delta Zwint}$*
160 mutant background. Abolishing the SAC aggravated the growth defect of the *kre28$^{\Delta Zwint}$* mutant,
161 an effect that was particularly apparent at temperatures of 25 °C and 16 °C (**Figure 2 B**). Thus,
162 the benomyl hypersensitivity of the *kre28$^{\Delta Zwint}$* mutant is not caused by a general mitotic
163 checkpoint defect, and indeed, the SAC is required to support viability of this mutant.
164 While *kre28$^{\Delta Zwint}$* mutant cells arrested efficiently in response to nocodazole, we found that
165 they nevertheless very quickly lost viability when cells were plated from nocodazole-containing
166 medium onto YEPD plates (**Figure 2 - Supplement**). To determine the reason for the rapid
167 loss in viability we arrested wildtype and mutant cells with nocodazole, then washed out the
168 drug to allow spindle reformation and chromosome attachment and followed the progression
169 through the first cell division. Analysis of Pds1 degradation kinetics showed that *kre28$^{\Delta Zwint}$*
170 mutant cells initiated anaphase – indicated by the decline in Pds1 levels - with the same timing
171 as wildtype cells **(Figure 2 C**). The lack of a delay indicated that the SAC was not activated
172 under these conditions. In the same experimental setup, we analyzed the distribution of
173 fluorescently labelled chromosome XII (CEN12-GFP) following the nocodazole washout
174 (**Figure 2 D**). Strikingly, *kre28$^{\Delta Zwint}$* mutant cells missegregated chromosome XII in nearly 70 %
175 of all anaphases, while wildtype cells displayed an error rate of less than 5% (**Figure 2 E)**. This
176 high rate of missegregation can explain the pronounced benomyl hypersensitivity and the rapid
177 loss of viability after exposure to nocodazole.

178 The combination of phenotypes displayed by the *kre28$^{\Delta Zwint}$* mutant - a functional SAC in
179 response to microtubule depolymerization, but pronounced chromosome missegregation
180 without checkpoint activation following spindle reformation - is reminiscent of mutants in the
181 tension-dependent error correction pathway, such as *ipl1*, *sli15* or *sgo1* [41,42]. In genetic crosses
182 we found that the *kre28$^{\Delta Zwint}$* mutant was highly sensitive to further perturbations of the error
183 correction machinery: Its combination with the temperature-sensitive *ipl1-1* allele resulted in

184 extremely poorly growing spores (**Figure 2 F**) and its combination with *sli15-3* or *sgo1Δ* was
185 synthetic lethal. The genetic interactions of the *kre28*$^{\Delta Zwint}$ allele are summarized in **Figure 2 G**.
186 Deletion of the Kre28 Zwint helix is synthetically lethal or aggravates growth defects when the
187 function of the microtubule-binding Ndc80 complex (*ndc80-1*) and Dam1 complex (*dam1-1*,
188 *dam1-9* and *duo1*$^{\Delta SxIP}$) is compromised. Furthermore, either direct perturbation of the CPC
189 (*ipl1-1* and *sli15-3*) or affecting its centromere (*sgo1Δ*) or inner kinetochore recruitment
190 pathways (*ctf19*$^{\Delta C\text{-}RWD}$) dramatically reduced cell growth in combination with the *kre28* mutant
191 allele.
192

193 **The *kre28*$^{\Delta Zwint}$ mutant reduces the level of Spc105/Kre28 at kinetochore clusters *in vivo***
194 To further define the molecular basis of the *kre28*$^{\Delta Zwint}$ phenotype, we analyzed outer
195 kinetochore composition in wildtype and mutant cells by live cell imaging. The fluorescence
196 intensity of the KMN components Nuf2-GFP (Ndc80 complex) and Mtw1-GFP (Mtw1 complex)
197 at metaphase and anaphase kinetochore clusters was unaffected by the *kre28*$^{\Delta Zwint}$ mutation
198 (**Figure 3 A**). By contrast, we noticed a reduction of Spc105-GFP intensity at metaphase
199 kinetochores to about 70 % of the wildtype level and found that the apparent increase in cluster
200 intensity between metaphase and anaphase was reduced relative to the wildtype (**Figure 3 B**).
201 These differences were not caused by changes in protein levels, as judged by western blotting
202 (**Figure 3 – Supplement A**). Since we found that a C-terminal GFP fusion caused a reduced
203 protein level of the *kre28*$^{\Delta Zwint}$ mutant (**Figure 3 – Supplement C and D**), we constructed and
204 analyzed N-terminal GFP-fusions of wildtype and mutant alleles. GFP-Kre28$^{\Delta Zwint}$ was present
205 at near wildtype levels in western blots (**Figure 3 – Supplement B).** Similar to Spc105-GFP,
206 the GFP-*kre28*$^{\Delta Zwint}$ mutant displayed a moderate reduction in metaphase kinetochore cluster
207 intensity and a less pronounced increase in apparent anaphase cluster intensity (**Figure 3 B**).
208 We conclude that the *kre28*$^{\Delta Zwint}$ mutation has a specific effect on the KMN network *in vivo*: It
209 reduces the localization of Spc105/Kre28 to kinetochores without affecting the recruitment of
210 Ndc80 and Mtw1 complexes.
211 Since Spc105 acts as a scaffold for the Mps1-dependent recruitment of Bub1/Bub3, we asked
212 if the Spc105 reduction would have any consequences on downstream signaling. We found
213 that Sgo1-GFP localization to kinetochores in prometaphase (which is dependent on Bub1)
214 was not affected by *kre28*$^{\Delta Zwint}$, suggesting that the modest reduction in Spc105 does not have
215 a pronounced effect on downstream signaling (**Figure 3 – Supplement E**). This is also
216 consistent with the observation that this mutant has a functional SAC.
217 Using recombinant expression of all ten KMN subunits in Sf9 cells, we found that affinity
218 purification via Spc105-Flag allowed the isolation of the entire yeast KMN network independent
219 of whether Kre28 was in wildtype or ΔZwint mutant form (**Figure 3 C**). Upon prolonged

220 incubation of recombinant KMN on beads, however, Mtw1c and Ndc80c subcomplexes
221 dissociated more easily from the Spc105/Kre28$^{\Delta Zwint}$ mutant KMN network (**Figure 3 C and D,**
222 **see also Figure 4 – Supplement 2 A**). In line with the *in vivo* observations, these experiments
223 therefore indicate that the *kre28* $^{\Delta Zwint}$ mutation reduces the affinity between the Spc105/Kre28
224 and the Mtw1c/Ndc80c subcomplexes of the KMN network.

225

226 **Ipl1/Sli15 directly binds the KMN network via the Spc105/Kre28 subcomplex**

227 Since the *kre28*$^{\Delta Zwint}$ allele reduced the association of Spc105/Kre28 with kinetochores in cells
228 and phenotypically resembled mutants in the error correction pathway, we asked whether the
229 Ipl1/Sli15 complex may directly associate with the KMN network and specifically with
230 Spc105/Kre28. To this end we co-expressed the ten KMN subunits from two separate
231 baculoviruses in Sf9 insect cells and purified the network via a Flag tag at the C-terminus of
232 the Spc105 subunit. This purification strategy allowed the single-step isolation of a stable full-
233 length KMN network that co-eluted stoichiometrically during analytical size exclusion
234 chromatography (SEC) (**Figure 4 A**). We evaluated the organization of the KMN network by
235 Pt/C rotary shadowing electron microscopy. In electron micrographs the Ndc80 complex (N)
236 was readily identifiable as a 50-60 nm long rod and its distal end was decorated by one or two
237 appendages – formed by the KM complexes - which seemed to adopt a variety of different
238 conformations relative to each other (**Figure 4 B**).

239 We then incubated the recombinant KMN network immobilized on anti-Flag M2 beads with
240 bacterially expressed Ipl1/6xHis-Sli15 (**Figure 4 C**). Western blotting indicated that our
241 Ipl1/6xHis-Sli15 preparation contained two major forms of Sli15, both recognized by the anti-
242 His antibody. The faster migrating form is therefore a C-terminal truncation of Sli15. This
243 fragment can be purified away from full-length Sli15 and is unable to bind Ipl1 since it lacks the
244 IN box (**Figure 4 – Supplement 1 B**). We found that wildtype Kre28 and Kre28$^{\Delta Zwint}$ KMN
245 networks, but not empty control beads, bound the Ipl1/Sli15 complex in the pull down
246 experiment. Interestingly, preferentially the full length Sli15 form was detected in the pull down
247 (**Figure 4 C**). Whereas Ipl1/Sli15 appeared to bind equally well to both wildtype and mutant
248 KMN networks, the association of Mtw1c/Ndc80c to Spc105/Kre28 was slightly reduced in the
249 Kre28 $^{\Delta Zwint}$ mutant, as discussed before (**see Figure 4 C**). Changing the pull down protocol to
250 prolonged incubation times, led to a more complete dissociation of Mtw1c/Ndc80c from
251 Spc105/Kre28, while Ipl1/Sli15 binding was largely preserved (**Figure 4 – Supplement 2 A**).
252 Kinase assays showed that Spc105, Ndc80 and Dsn1 were major KMN substrates of Ipl1, as
253 anticipated from previous work [43]. Interestingly, Ipl1 autophosphorylation - a readout for its
254 activity - appeared to be increased in the presence of the KMN network (**Figure 4 –**
255 **Supplement 2 B and C**).

256 We next compared the ability of Ipl1/Sli15 to bind to the different subcomplexes of the KMN
257 network by immobilizing Spc105-Flag/Kre28 (K subcomplex) or Mtw1c/Ndc80c-Flag (MN
258 subcomplexes) separately on anti-Flag M2 beads. Western blotting showed that Ipl1/Sli15
259 interacted exclusively with Spc105/Kre28, but not with Ndc80c/Mtw1c under these conditions
260 (**Figure 4 D**).
261 Our initial characterization showed that the Ipl1/Sli15 complex was autophosphorylated
262 following expression and purification from *E. coli* (**Figure 4 - Supplement 1 A**). We tested the
263 effect of Ipl1 autophosphorylation on the binding to immobilized Spc105/Kre28 by comparing
264 an untreated control with samples including either ATP (to promote phosphorylation) or
265 Lambda phosphatase (to eliminate phosphorylation). We found that inclusion of ATP strongly
266 reduced the association of Ipl1/Sli15 with Spc105/Kre28, while addition of Lambda
267 phosphatase promoted binding (**Figure 4 E**). Judged by protein band intensity, near
268 stoichiometric amounts of Ipl1 seemed to bind to immobilized Spc105/Kre28 in the untreated
269 or Lambda phosphatase-treated sample. Thus, we conclude that Ipl1/Sli15 binds recombinant
270 KMN *in vitro* via the Spc105/Kre28 complex and that this interaction can be counteracted by
271 Ipl1 autophosphorylation.
272 Unlike the checkpoint kinase Mps1, the Ipl1/Sli15 kinase complex is typically not recovered as
273 a stable component of kinetochore purifications from yeast extracts using Dsn1-Flag [44]. Using
274 a proximity-dependent *in vivo*-biotinylation approach with the TurboID Ligase [45] we found,
275 however, that Sli15-6xFlag could be detected in Streptavidin affinity-purifications from extracts
276 of strains that expressed Spc105-TurboID, similar to the constitutive Spc105 binding partner
277 Kre28 (**Figure 4 F**). By contrast, the nuclear kinesin-5 motor protein Cin8, implicated in the
278 regulation of kinetochores via Ndc80 [46,47], was not recovered with Spc105-TurboID, despite
279 similar input levels in extracts. This supports the idea that Spc105-Sli15 interactions also occur
280 *in vivo*, although possibly only transiently.
281 To characterize the KMN-Ipl1/Sli15 assembly in more detail, we conducted chemical
282 crosslinking with the homobifunctional amine-to-amine crosslinker BS3, followed by mass
283 spectrometry (XL-MS). The resulting Lys-Lys proximity map is in overall agreement with the
284 established KMN subunit topology (**Figure 5 A and B**). In particular it showed that the C-termini
285 of the subunits Mtw1, Dsn1 and Nsl1 are closely connected to each other and proximal to
286 Spc105/Kre28 and to the Spc24/Spc25 heterodimer of the Ndc80 complex[8,19,21]. The majority
287 of Sli15/Ipl1 crosslinks to the KMN network is found on the Spc105-Kre28 subcomplex (17
288 different crosslinks to Spc105/Kre28, 4 to Mtw1c and 4 to Ndc80c). In particular, the Spc105
289 segment 450-700, encompassing the helical bundle and the coiled-coil with Kre28, is found in
290 proximity to Sli15. Overall, these crosslinks are consistent with the binding experiments,
291 showing that Spc105/Kre28 is the main interaction partner of Ipl1/Sli15 in the outer kinetochore
292 KMN network.

293

294 **Artificial recruitment of Ipl1 to Mtw1 suppresses the *kre28$^{\Delta Zwint}$* phenotype *in vivo***

295 If the *kre28$^{\Delta Zwint}$* mutant reduces the association of Spc105/Kre28 to kinetochores *in vivo* and
296 an important role of this complex is to bind and position Ipl1/Sli15, then artificially increasing
297 Ipl1 recruitment in the mutant may rescue the defect (**Figure 6 A**). We tested this hypothesis
298 by constructing fusion proteins between the Mtw1 subunit (whose kinetochore level is
299 unaffected by *kre28$^{\Delta Zwint}$*, **Figure 3 A**) and different C-terminal segments of the Sli15 protein.
300 The fusions were either prepared with wildtype Sli15 sequences or with two point mutations
301 exchanging conserved amino acids in the IN box (W646G, F680A), which prevent Ipl1
302 binding[33]. The genes encoding the fusion proteins were integrated as extra copies at the *lys2*
303 locus and expressed constitutively under control of the *MTW1* promoter (**Figure 6 B, Figure 6**
304 **- Supplement**).

305 Serial dilution assays showed that expression of neither fusion protein alone caused any
306 growth defects in a Kre28^{WT} strain background. Interestingly, Mtw1-Sli15$^{565-698}$ improved
307 growth of the *kre28$^{\Delta Zwint}$* mutant in the presence of benomyl. Moreover, the longer Mtw1-
308 Sli15$^{516-698}$ fusion, encompassing the IN box and the single alpha helix (SAH) domain, was
309 even more effective in suppressing the benomyl hypersensitivity of the *kre28$^{\Delta Zwint}$* mutant.
310 Importantly, fusion proteins with point mutations in the IN box had no beneficial effect on growth
311 of *kre28$^{\Delta Zwint}$* strains in the presence of benomyl, demonstrating the importance of Ipl1
312 recruitment to the outer kinetochore.

313 We further analyzed the effect of the two Mtw1-Sli15 fusions on *kre28$^{\Delta Zwint}$* cells by scoring
314 segregation of fluorescently labelled chromosome XII in the first division after release from a
315 nocodazole arrest. As described before (see **Figure 3 E**) about 70 % of *kre28$^{\Delta Zwint}$* cells
316 missegregated chromosome XII. In contrast, the rate of missegregation was significantly
317 reduced in *kre28$^{\Delta Zwint}$* cells expressing the Mtw1-Sli15 fusion proteins (**Figure 6 D**). Similar to
318 the effect in the serial dilution assay, expression of the larger construct comprising Sli15
319 residues 516-698 showed a stronger suppression of the *kre28$^{\Delta Zwint}$* phenotype. Notably,
320 constitutive recruitment of Ipl1 the outer kinetochore via the Mtw1 fusion had no negative effect
321 on chromosome biorientation in a wildtype strain background.

322 These data indicate that an outer kinetochore pool of Ipl1/Sli15 recruited by Spc105/Kre28 has
323 a crucial role in establishing chromosome biorientation and that a lack of Ipl1/Sli15 at the outer
324 kinetochore is a main cause of the phenotypes observed in *kre28$^{\Delta Zwint}$* strains.

325

326 **The N-terminus of Ipl1 is implicated in outer kinetochore recruitment by KMN**

327 We asked how an interaction between Ipl1/Sli15 and the KMN network may be established at
328 the molecular level. Since a C-terminal Sli15 truncation lacking the IN box seemed to be less

329 effective in binding KMN *in vitro* (**Figure 4 C**), we reasoned that the Ipl1 kinase itself might
330 contribute to the interaction. Ipl1 can be subdivided into a C-terminal globular kinase domain
331 (residues 96-385) and a largely unstructured N-terminus (residues 1-95). We have previously
332 shown that the Ipl1 N-terminus establishes binding to the yeast end-binding (EB) protein Bim1,
333 contributing to the spindle localization of the CPC in anaphase [48]. In addition, recent
334 experiments have reported interactions between peptides derived from the Ipl1 N-terminus and
335 Ndc80/Nuf2 [18], suggesting the presence of outer kinetochore binding motifs in this segment of
336 Ipl1 (**Figure 7 A**). Interestingly, AlphaFold2 reproducibly predicted an interaction between Ipl1
337 residues 1-30 and the Spc105/Kre28 helical bundle **(Figure 7 B**; Supplement). This Ipl1
338 segment includes a predicted alpha helix, and is well conserved among yeast aurora kinases,
339 even better than the more carboxyterminal segment involved in Bim1 or Ndc80/Nuf2 binding
340 (**Figure 7 A**). Closer inspection of the predicted binding interface suggests crucial roles for Ipl1
341 residues Leu11, Arg23 and Ile29. We produced a recombinant Ipl1-(L11A R23A I29A)/6xHis-
342 Sli15 complex in *E.coli* and performed pull down experiments with Spc105-Flag/Kre28 *in vitro*.
343 We found that the Ipl1-3A mutation reduced the amount of Sli15 in the pull down relative to
344 wildtype, but did not abolish it completely (**Figure 7 C**).

345 If the N-terminus of Ipl1 was indeed involved in crucial functions during mitotic error correction,
346 we would expect mutations or truncations to cause growth defects. To test this prediction, we
347 replaced one *IPL1* allele in diploid cells with Flag-tagged wildtype *IPL1*, the *ipl1-3A* point
348 mutant, or different N-terminal truncations. Upon sporulation and dissection, we evaluated the
349 viability and growth phenotypes of the haploid strains. In otherwise wildtype strains, the *ipl1* N-
350 terminal point- or truncation mutants fully supported viability and exhibited no obvious growth
351 defects (**Figure 7 E-G**). We reasoned that fully intact centromere-dependent recruitment
352 pathways may mask the contributions of the Ipl1 N-terminus (**Figure 7 D**). We therefore
353 conditionally depleted Sgo1 in Ipl1 wildtype cells or N-terminal mutants using an auxin-
354 inducible degron. While wildtype Ipl1 supported viability when Sgo1 was depleted (+Galactose,
355 +NAA), the *ipl1*^{3A} mutant displayed a growth defect under the same conditions **(Figure 7 E**).
356 Moreover, *ipl1* truncation mutants were unable to support viability, quickly giving rise to
357 individual larger colonies, which likely represent suppressors. Thus, depletion of Sgo1 greatly
358 sensitizes cells for mutations in the Ipl1 N-terminal tail. Recent studies have shown that the
359 inner kinetochore COMA complex directly interacts with Ipl1/Sli15 and can therefore configure
360 a Bir1-independent pathway to recruit the kinase to the kinetochore [36,37]. The C-terminal RWD
361 domain of Ctf19 is required for the interaction with Sli15/Ipl1 *in vitro* [36]. We therefore combined
362 *ipl1* N-terminal mutants with *ctf19*$^{\Delta RWD\text{-}C}$. We note that the Ctf19$^{\Delta RWD\text{-}C}$ protein is still able to
363 interact with Mcm21, and therefore constitutes a less severe allele than *ctf19Δ*. Evaluation of
364 the genetic crosses and the resulting haploid yeast strains showed that *ipl1* N-terminal mutants
365 did not display growth defects in *CTF19* wildtype strains. By contrast, *ipl1* N-terminal

366 truncations Δ2-30 and Δ2-55 conferred poor growth in *ctf19*$^{\Delta RWD\text{-}C}$ cells (**Figure 7 F**). In
367 addition, *ipl1* point mutants and N-terminal truncations greatly aggravated the benomyl-
368 hypersensitivity of *ctf19*$^{\Delta RWD\text{-}C}$. Overall, these results reveal an important function for the Ipl1
369 N-terminus when centromere or inner kinetochore recruitment pathways of the CPC are
370 compromised.

371

372 **Discussion**

373 **New *kre28* mutant alleles reveal specific contributions to outer kinetochore function**

374 While the molecular roles of Ndc80c and Mtw1c complexes in the kinetochore architecture are
375 well established, the functional contributions of Spc105/Kre28 still await further definition. The
376 mitotic checkpoint function of Spc105 is well understood, but it cannot account for its essential
377 role in budding yeast. The *kre28*$^{\Delta Zwint}$ allele described in this study can be used to reveal
378 additional aspects of Spc105/Kre28 function. We show that it causes a selective reduction of
379 Spc105/Kre28 at the kinetochore without affecting the levels of Ndc80 and Mtw1 complexes.
380 It is therefore much more selective than more penetrant perturbations. For example, a
381 depletion or reduction of human Knl1 by RNAi strongly affects the levels of additional outer
382 kinetochore components such as Ndc80/Hec1 as well [49,50], making it difficult to delineate a
383 specific function. We note that the observed Spc105/Kre28 reduction in metaphase cells is
384 moderate and does not lead to impaired spindle assembly checkpoint activity, as the mutant
385 cells are fully capable of arresting in nocodazole. In addition, they show normal levels of Sgo1
386 recruitment to the kinetochore in prometaphase, suggesting sufficient Bub1 activity at the
387 kinetochore. We currently cannot provide a precise molecular explanation for why the
388 mutations in the Kre28 helical bundle may reduce the affinity of Spc105/Kre28 for
389 Ndc80c/Mtw1c, both *in vivo* and *in vitro*. Even though AlphaFold2 models predict multiple
390 possible conformations of KMN, they do not show a binding interface within KMN that would
391 include the Kre28 Zwint helix. It seems possible that the mutation causes a structural defect in
392 the organization of the Spc105/Kre28 heterodimer that lowers its affinity to MN.
393

394 **An outer kinetochore recruitment mechanism for the Ipl1/Sli15 kinase complex**

395 Taken together, four lines of evidence support the conclusion that the *kre28* helical bundle
396 mutant phenotype is caused by insufficient Ipl1 activity at the outer kinetochore.

397 1. The phenotypes of the *kre28*$^{\Delta Zwint}$ mutant strongly resemble defects in the tension-dependent
398 error correction pathway. The mutant cells have a functional mitotic checkpoint in response to
399 nocodazole, but when forced to reassemble a spindle following nocodazole withdrawal, they
400 ignore biorientation problems and missegregate chromosomes without delaying the initiation
401 of anaphase. The lack of a delay indicates that the cells can form kinetochore-microtubule
402 attachments, because otherwise the unattached kinetochores would activate the checkpoint.
403 This characteristic behavior is also displayed by *sgo1* mutants [42] and indicates an inability to
404 sense the incorrect attachment status.

405 2. The genetic interaction profile indicates that the *kre28* mutant is very sensitive to further
406 perturbations of Ipl1/Sli15, its recruitment pathways, or mutations in its outer kinetochore
407 substrates.

408 3. The *kre28*$^{\Delta Zwint}$ mutant is suppressed by artificial recruitment of Ipl1 via an Mtw1-Sli15 fusion
409 protein. We show that the Mtw1-Sli15 fusion can only suppress the phenotype when capable
410 of binding Ipl1. We suspect that fusing the Sli15 segment to the C-terminus of Mtw1
411 reintroduces Ipl1 at the proper location within KMN, while previous studies report constitutive
412 Sli15 fusions to Ndc80 to be incompatible with biorientation[51]. Our live cell imaging experiment
413 using fluorescently labelled chromosomes demonstrates that an improved chromosome
414 segregation after nocodazole washout is the basis for the suppression of the growth defect.
415 4. Recombinant Ipl1/Sli15 binds KMN via the Spc105/Kre28 subunits *in vitro*. The crosslink-
416 mass spectrometry experiments are consistent with Spc105/Kre28 providing the main binding
417 site within the KMN network. Autophosphorylation of Ipl1/Sli15 inhibits binding, possibly
418 preventing excessive Ipl1 recruitment which would hinder the re-establishment of kinetochore-
419 microtubule attachments during error correction. Our findings are consistent with earlier reports
420 showing that depletion of Knl1 appears to reduce Aurora B substrate phosphorylation in human
421 cells [49].
422
423 **Implications for the tension-sensing mechanism of the outer kinetochore**
424 Our results indicate that the Ipl1 kinase module of the CPC is an integral part of the outer
425 kinetochore and can therefore be influenced by architectural and conformational changes that
426 occur in different attachment situations. This is compatible with the previously proposed model
427 that CPC centromere anchoring generates a gradient of Aurora B activity and that tension pulls
428 substrates out of the reach of the kinase[52]. The structure of the Sli15 protein with the
429 centromere localization module at the N-terminus and the kinase module at the C-terminus
430 should allow a single CPC molecule to simultaneously bind to both locations (**Figure 8 A**).
431 Alternatively, a separate pool of Ipl1/Sli15 may bind the outer kinetochore independently of the
432 centromere-targeting subunits Bir1/Nbl1.
433 Structure predictions, our biochemical experiments and the recent report of an Ipl1 peptide
434 bound to the Ndc80/Nuf2 head [18] implicate the N-terminal domain of Ipl1 in the outer
435 kinetochore recruitment mechanism. We have previously demonstrated that the N-terminus
436 binds budding yeast Bim1^{EB1} via two SxIP motifs (residues 46-49 and 72-75) in this domain[48],
437 which promotes the relocalization of Ipl1 to the spindle midzone in anaphase, where it
438 contributes to timely spindle disassembly [53,54]. Interestingly, the presence of adjacent binding
439 motifs for Kre28/Spc105 and Ndc80c in the Ipl1 -N-terminus would mean that simultaneous
440 binding should only occur when the Ndc80/Nuf2 head and the Kre28/Spc105 helical bundle
441 come into close proximity to each other (**Figure 8 B**). Docking of the kinase module onto
442 Spc105/Kre28 could then facilitate Ndc80 phosphorylation and prevent premature Dam1c
443 association under low tension conditions when the Ndc80 head can adopt conformations close
444 to the Spc105/Kre28 helical bundle. Upon establishment of tension, microtubule-generated

445 forces may change the distance between these binding sites and decrease the affinity of
446 Ipl1/Sli15 for the outer kinetochore or its activity (**Figure 8 B**). This concept of conformation-
447 sensitive kinase docking could make an important contribution to the tension-sensing
448 mechanism. Our genetic experiments show that the Ipl1 N-terminus is not required for viability
449 in otherwise wildtype cells, but its contribution is unmasked when the centromere/kinetochore
450 targeting pathways of the CPC are compromised. Future experiments will have to develop
451 quantitative binding assays to better characterize the contributions of different CPC binding
452 interfaces within KMN. The basis for the sensitivity of KMN recruitment to autophosphorylation
453 will also need to be investigated in more detail. In addition to the Ipl1 N-terminus, the
454 crosslinking data also implicate Sli15 in outer kinetochore binding, a contribution which will
455 need to be characterized in future experiments as well.
456 The *kre28*$^{\Delta Zwint}$ mutation is very sensitive to perturbations of the CPC inner kinetochore
457 recruitment pathway, which would suggest that an outer kinetochore docking mechanism alone
458 cannot provide full functionality. We note, however, that the severity of the *kre28*$^{\Delta Zwint}$
459 phenotype indicates that outer kinetochore docking of the kinase module could make a very
460 important contribution to CPC function during error correction. It could also explain why
461 reconstituted kinetochore-microtubule attachments remain tension-sensitive to Ipl1/Sli15
462 constructs lacking the CEN localization module [43]. Future experiments will have to investigate
463 how Ipl1 kinase activity towards key substrates may be influenced by distinct KMN
464 conformations under force.
465
466

467 ## Material and methods

468 ### Cultivation and genetic manipulation of yeast

469 All yeast strains used in this study are based on the S288C strain. Standard techniques were
470 used for cultivation and genetic manipulation of yeast strains. PCR-generated integration
471 cassettes were generated as described in Longtine *et al*, 1998 and Janke *et al*, 2004.
472 Alternatively, linearized plasmids with ends homologous to the site of integration were used for
473 transformation. Plasmids used for yeast transformation are listed in Table 1.

474

Name	Coding sequence
pAD77	Kre28^{WT}-6xFlag in pRS306
pAD78	Kre28$^{\Delta Zwint}$-6xFlag in pRS306
pJP1	Kre28$^{\Delta 77-90}$-6xFlag in pRS306
pJP2	Kre28$^{\Delta 91-102}$-6xFlag in pRS306
pJP3	Kre28$^{\Delta 103-113}$-6xFlag in pRS306
pAD81	Kre28^{4A}-6xFlag (L95A, K96A, Y99A, E101A) in pRS306
pAD82	Kre28^{3A}-6xFlag (E103A, L105A, D106A) in pRS306
pAD84	Kre28^{6A}-6xFlag (F108A, F109A, R110A, F111A, T112A, L113A) in pRS306
pAD89	Kre28^{WT}-GFP in pRS306
pAD90	Kre28$^{\Delta Zwint}$-GFP in pRS306
pAD98	Mtw1-6xHA-Sli15$^{565-698}$ in pRS307
pAD101	GFP-Kre28^{WT}-6xFlag in pRS306
pAD102	GFP-Kre28$^{\Delta Zwint}$-6xFlag in pRS306
pAD103	Kre28$^{\Delta RWD}$-6xFlag in pRS306
pAD104	Kre28$^{\Delta Zwint\ \Delta RWD}$-6xFlag in pRS306
pAD105	Mtw1-6xHA-Sli15$^{565-698}$ (W646G, F680A) in pRS307
pAD108	Mtw1-6xHA-Sli15$^{516-698}$ in pRS307
pAD118	Mtw1-6xHA-Sli15$^{516-698}$ (W646G, F680A) in pRS307
pAD120	Mtw1-6xHA-Sli15$^{565-698}$::natNT2 in pRS307
pAD121	Mtw1-6xHA-Sli15$^{516-698}$::natNT2 in pRS307
pAD126	Ipl1 (L11A, R23A, I29A)/6xHis-Sli15 in pETDuett
pSW574	Ipl1-WT-2xFlag in pRS305
pAD127	Ipl1 (L11A, R23A, I29A)-2xFlag in pRS305
pAD129	Ipl1 Δ2-30-2xFlag in pRS305
pLP1	Ipl1 Δ2-55-2xFlag in pRS305

475

476 **Table 1**: List of plasmids used in this study

477

478

479 ### Sporulation and dissection of diploid yeast strains

480 Cells from 1 ml of a saturated overnight culture of diploid yeasts strains were washed twice
481 with 1 ml ddH_2O, resuspended in 4 ml sporulation medium and incubated at room temperature
482 for several days until tetrads were formed. 250 µl of the sporulation culture were centrifuged
483 and the cell pellet was resuspended in 37.5 µl Zymolase T (1 mg/ml) and incubated at 37 °C
484 for 3.5 minutes. Afterwards, 200 µl of cold 100 mM potassium phosphate buffer (pH 7.0) was
485 added. A few microliters of the cell suspension were streaked out on a YEPD plate and tetrads

486 were dissected using a Singer MSM semi-automated dissecting microscope. Plates were
487 incubated at 30 °C for three days. For genotyping, the spores were resuspended in minimal
488 medium and spotted on YEPD, drop-out and mating type tester plates.
489

490 **Serial dilution assay**

491 Cells from a saturated overnight culture were diluted to OD_{600} = 0.4 in minimal medium and
492 serially diluted (1:4, six dilution steps in total). Cells were spotted on YEPD or YEPD + benomyl
493 (20 µg/ml; Sigma-Aldrich) plates using a pinning tool. Plates were incubated at 25 °C, 30 °C
494 or 37 °C for two days or at 16 °C for five days.
495

496 **Preparation of western blot samples from yeast cultures**

497 Samples for western blot analysis were prepared according to a protocol adapted from [55]. In
498 brief, an equivalent of 2 OD_{600} from a logarithmically growing culture was harvested by
499 centrifugation, resuspended in 100 µl ddH_2O and 100 µl 0.2 M NaOH was added. Samples
500 were incubated at room temperature for five minutes, cells were pelleted, resuspended in 50 µl
501 SDS-PAGE loading buffer and boiled at 95 °C for five minutes. 6 – 8 µl of sample were loaded
502 for SDS-PAGE. Proteins were transferred to a Amersham™ Protran™ Nitrocellulose Blotting
503 Membrane (Cytiva) by wet transfer. Membranes were blocked in TBST with 5 % (w/v) skimmed
504 milk, incubated with the respective antibodies listed in Table 2 and membranes were washed
505 in TBST. For detection of signals from HRP-conjugated antibodies, membranes were
506 incubated with ECL™ (Prime) Western Blotting Detection Reagents (Cytiva). Signals were
507 visualized using an Amersham Imager 600 (GE Healthcare).
508

name	species	manufacturer	product number	dilution
anti-Flag (HRP-conjugated) (M2)	mouse	Sigma-Aldrich	A8592	1:10000
anti-HA	mouse	Biolegend	901514	1:1000
anti-Myc (9E10)	mouse	Santa Cruz Biotechnology, Inc	sc-40	1:1000
anti-GFP	mouse	Roche	11814460001	1:1000
anti-Pgk1 (22C5D8)	mouse	Invitrogen	459250	1:5000
anti-penta-His (HRP-conjugated)	mouse	Qiagen	34460	1:5000
anti-mouse IgG (HRP-conjugated)	sheep	Cytiva	NA931V	1:10000

509

510 **Table 2**: List of antibodies used in this study

511

512

513 **Analysis of cell cycle progression after release from α factor arrest into medium with**
514 **nocodazole**
515 Cells from a saturated overnight culture were diluted to OD_{600} = 0.2 and incubated at 30 °C
516 from 1 hour. α factor was added to a final concentration of 10 µg/ml and cells were further
517 incubated at 30 °C for 2 – 2.5 hours. Arrest in G1 phase was confirmed by microscopy when
518 more than 90 % of cells had a shmoo. Cells were subsequently collected by centrifugation,
519 washed two times with pre-warmed YEPD supplemented with 100 µg/ml pronase (Roche) and
520 once with pre-warmed YEPD without pronase. Cells were resuspended in pre-warmed YEPD
521 with 15 µg/ml nocodazole (Sigma) and further cultivated at 30 °C. Samples for western blot
522 analysis were taken immediately and every 30 minutes after release from the α factor arrest.
523
524

525 **Analysis of cell cycle progression after release from a nocodazole arrest**
526 Cells from a saturated overnight culture were diluted to OD_{600} = 0.2 and grown at 30 °C for
527 1.5 hours. Nocodazole was added to a final concentration of 15 µg/ml, followed by further
528 incubation at 30 °C for 2 hours. Arrest in mitosis was confirmed by microscopy when more than
529 90 % of cells were large budded. Cells were harvested by centrifugation, washed three time
530 with pre-warmed YEPD, resuspended in pre-warmed YEPD with 10 µg/ml α factor to arrest
531 cells in the next G1 phase and further cultivated at 30 °C. Samples for western blot analysis
532 were collect every 15 minutes after release from the nocodazole arrest.
533

534 **Viability assay after nocodazole treatment**
535 Cells from a saturated overnight culture were diluted to OD_{600} = 0.2 and incubated at 30 °C for
536 3 hours. Nocodazole was added to a final concentration of 15 µg/ml and cultures were further
537 incubated at 30 °C for 1.5 hours. Before and after nocodazole treatment, an aliquot was taken
538 from the cultures and serially diluted to OD_{600} = 0.0004. 100 µl of the diluted culture were plated
539 on YEPD plates and incubated at 30 °C for two days. The number of colonies grown on each
540 plate was counted. For each strain, the number of colonies formed in the untreated sample
541 was defined as 100 %.
542

543 **Live cell microscopy**
544 For live cell microscopy to quantify fluorescence signal intensities, cells from a saturated
545 overnight culture were diluted to OD_{600} = 0.2 in YEPD medium and grown at 30 °C for four to
546 five hours. Cells were then immobilized on glass bottom dishes (No 1.5, MatTek corporation)
547 coated with 0.1 mg/ml concanavalin A (Sigma) and the dish was filled with SD doTrp medium.
548 To analyze chromosome segregation after nocodazole washout, cells were diluted to

549 OD_{600} = 0.2 in YEPD medium and grown at 30 °C for two hours. Cells were treated with
550 15 µg/ml nocodazole, further incubated at 30 °C for 1.5 hours and then immobilized in multi
551 well glass bottom dishes (Ibidi) coated with 0.1 mg/ml concanavalin A (Sigma). The Cells were
552 washed three times with SD doTrp to wash out the nocodazole and the imaging chamber was
553 filled with SD doTrp. Images were acquired at 10 minutes intervals over a total time of 1.5 to
554 2 hours. All media were supplemented with 100 µM $CuSO_4$ to induce expression of LacI-GFP
555 which is under control of the Cup1 promoter.
556 All microscopy was performed with a DeltaVision Elite wide-filed microscope (GE Healthcare
557 Life Sciences) with a Super-Plan Apo 100x/1.4 oil objective, solid state light source (SSCI) and
558 sCMOS camera. Imaging was performed at 30 °C. Z-stacks with a spacing of 0.4 µm covering
559 a total distance of 6 µm were acquired and maximum projections were generated. Alternatively,
560 OAI (optical axis integration) scans over 6 µm were performed. Images were deconvolved
561 using the default settings of the SoftWoRx software (GE Healthcare Life Sciences).
562

563 **Quantification of fluorescence microscopy signal**

564 Fluorescence microscopy signals were quantified using Fiji. Equally sized boxes were drawn
565 around individual kinetochore clusters of metaphase or anaphase cells and the mean
566 integrated density was measured. Additionally, the local background in proximity to the
567 kinetochore cluster was measured and subtracted from the signal.
568 For each experimental data set, the mean value measured for metaphase kinetochore clusters
569 of the $Kre28^{WT}$ strain was defined as 1.0 as and all other data was normalized accordingly for
570 better comparison.
571

572 **Statistical analysis**

573 Data was analyzed and visualized using the statistics software GraphPad Prism 10. Mean
574 values +/- standard deviation (SD) are displayed. Information on sample size and applied
575 statistical tests are provided in the figure legends.
576

577 **Multiple sequence alignments and secondary structure prediction**

578 Multiple sequence alignments were performed with sequences of Kre28 proteins from different
579 yeast species or with sequences of Kre28 and Zwint related proteins from various eukaryotic
580 species were used.
581 Sequences from yeast species were aligned using the MAFFT multiple alignment tool [56].
582 Alignments were visualized in Jalview [57] with Clustal coloring and 50 % conservation threshold.
583

584 Secondary structure predictions of *S. cerevisiae* Kre28 and *H. sapiens* Zwint were generated

585 using the JPred4 server [58].

586

587 **ColabFold structure predictions**

588 The structure of the Spc105$^{490-917}$/Kre28 heterodimer in Figure 1 was predicted using Colabfold
589 (https://colab.research.google.com/github/sokrypton/ColabFold/blob/main/beta/AlphaFold2_a
590 dvanced.ipynb)[59] with the following parameters: msa_method=mmseqs2,
591 pair_mode=unpaired, cov=0, qid=0, max_msa=512:1024, subsample_msa=True,
592 num_relax=0, use_turbo=True, use_ptm=True, rank_by=pLDDT, num_models=5,
593 num_samples=1, num_ensemble=1, max_recycles=3, tol=0, is_training=False,
594 use_templates=False. The figures of the predicted structures were further processed using the
595 software ChimeraX[60]. pLDDT values were colored in ChimeraX. Visualization of the predicted
596 alignment errors was prepared by Colabfold.

597

598 **AlphaFold2 molecular modelling**

599 AlphaFold (AF) was used for all molecular modeling in the versions AF2 Multimer 3.2.1 [61] and
600 AF3 [62]. A general feature of AF2 Multimer is the higher sensitivity to intra- and intermolecular
601 interactions compared to the original AF2 [63].
602 For the model shown in Fig. 7, two sub-complexes were predicted: Firstly, a complex consisting
603 of i) the yeast Mis12 complex [MTW1 (UNIPROT P39731), NNF1 (P47149), NSL1 (Q12143),
604 and DSN1 residues 270-C (P40568)], ii) the Spc24/Spc25 complex (Q04477/P40014), and iii)
605 the Spc105/Kre28 complex [Spc105 residues 421-917 (P53148) and Kre28 (Q04431)].
606 Secondly, a complex of Spc105 residues 421-917, Kre28 full length, and Ipl1 residues 1-30
607 (UNIPROT P38991), called "SKI" in the following, was also predicted with AF2 and
608 superimposed onto the first complex to visualize the binding site of Ipl1 in context of the
609 putative complete complex. The fragments were superimposed with PyMOL (Schrödinger,
610 LLC), and the stitching points within the alpha-helices were relaxed using alpha-helical
611 geometry restraints using COOT [64]. In the final model, 66% of the residues had very reasonable
612 pLDDT scores above 70, 42% had scores above 80, i.e. were predicted at least as "confident",
613 and 8% of the residues scored above 90, i.e. with very high confidence. Corroborating the high
614 quality of the model, the "predicted alignment error" (PAE) plots consistently indicated well-
615 defined relative positions of the domains to each other **(Figure 7 -Supplement 1**).
616 A more detailed interface analysis of the "SKI" complex showed that although the pLDDT
617 scores of the Ipl 1-30 peptide were very low, the reproducibility within the 10 predicted models
618 was very good, and the PAE scores were very favourable (**Figure 7 -Supplement 2**).
619 Interestingly, prediction with AF3 yielded even worse pLDDT scores for the Ipl1 peptide
620 compared to AF2. In contrast, the Spc105/Kre28 coiled coil helices at the interface have very

621 high confidence. The point mutations L11A, R23A, and I29A were designed based on the AF2
622 prediction using manual inspection as well as PISA [65] analysis that highlighted L11, I29, R23,
623 and P24 as most stabilizing residues.
624 The binding mode of Ipl1 1-30 would be consistent with a loss or weakening of binding upon
625 Ipl1-autophosphorylation since the binding site is next to extensive negatively charged patches
626 on the Spc105/Kre28 surface. In addition, the Ipl1/AurB consensus phosphorylation site
627 sequence [R/K]x[T/S][I/L/V/S/T] would match S5 (RNSL) and T20,T21,T22 (KKTTT). S15
628 could be a Cdk1 site (SPS).

629

630 **Expression of recombinant proteins in *Sf9* insect cells**

631 KMN and individual KMN subcomplexes were expressed in Sf9 (*Spodoptera frugiperda*) insect
632 cells. Cells were infected with baculoviruses carrying expression constructs for the respective
633 protein complexes. Information about baculoviruses used in this study are listed in Table 3. For
634 expression of the ten subunit KMN network, cells were co-infected with KT1-5 and KT1-6. Sf9
635 cells were split to a cell density of 0.8 x 10^6 cells/ml and grown at 27 °C with gentle agitation.
636 Next day, cells were infected with the respective baculoviruses and harvested two to three
637 days after infection.

638

Name of Baculovirus	Encoded kinetochore subunits
pFAP10	Spc105-Flag, Kre28^{WT*}
pFAP10 mut	Spc105-Flag, Kre28$^{\Delta Zwint}$
KT1-5	Dsn1, Mtw1, Nnf1, Nsl1, Spc105-Flag
KT1-6	Ndc80, Nuf2, Spc24, Spc25, Kre28^{WT}
KT1-6 mut	Ndc80, Nuf2, Spc24, Spc25, Kre28$^{\Delta Zwint}$
Ndc80c-Flag	Ndc80-Flag, Nuf2, Spc24, Spc25
pFAP19	Dsn1, Mtw1, Nnf1, Nsl1

639 **Table 3**: List of baculoviruses used in this study

640

641 **Pull down assays**

642 For pull down assays using proteins expressed in Sf9 cells, cells were resuspended in
643 interaction buffer (25 mM HEPES pH 7.4, 200 mM NaCl, 1 mM $MgCl_2$, 2.5 % (v/v) glycerol,
644 0.01 % (v/v) Tween-20) supplemented with 1 mM PMSF and Pierce™ Protease Inhibitor
645 (EDTA-free; ThermoFisher Scientific) and lysed by sonication. Lysates were cleared by
646 centrifugation. Anti-Flag M2 agarose beads (Sigma-Aldrich) were preequilibrated with
647 interaction buffer and incubated with the cleared lysate overnight, rotating at 4 °C. Afterwards,
648 beads were washed three times for 5 minutes with interaction buffer and loaded beads were
649 split into individual pull down samples.
650 To test for binding of Ipl1/Sli15 or Ipl1 to KMN or individual subcomplexes, 100 µl of 2 µM
651 Ipl1/Sli15 or Ipl1 was added to approximately 20 µl of loaded beads. As controls, Ipl1/Sli15 or

652 Ipl1 was also added to unloaded beads or loaded beads were incubated with interaction buffer
653 without any protein. 20 µl of the assembled reactions was taken as input samples for SDS-
654 PAGE analysis. Pull down samples were subsequently incubated rotating at 4 °C for 6 h.
655 Afterwards, beads were collected by centrifugation, the supernatant was removed, and the
656 beads were washed three times with 200 µl interaction buffer. Proteins bound to the beads
657 were eluted by addition of 50 µl interaction buffer with 0.5 or 1.0 µg/µl 3xFlag peptide, followed
658 by incubation at 4 °C for one to two hours.
659

660 ***In vitro* KMN stability assay**

661 Sf9 cells expressing KMN with either Kre28^{WT} or Kre28$^{\Delta Zwint}$ were resuspended in interaction
662 buffer (25 mM HEPES pH 7.4, 200 mM NaCl, 1 mM $MgCl_2$, 2.5 % (v/v) glycerol, 0.01 % (v/v)
663 Tween-20) supplemented with 1 mM PMSF and Pierce™ Protease Inhibitor (EDTA-free;
664 ThermoFisher Scientific) and lysed by sonication. Lysates were cleared by centrifugation,
665 added to M2 anti-Flag agarose beads (Sigma-Aldrich) preequilibrated with interaction buffer
666 and incubated overnight rotating at 4 °C. Next day, beads were washed three times for five
667 minutes with 1 ml interaction buffer and 730 µl interaction buffer was added to the beads.
668 Samples were collected immediately and 3, 6 and 24 hours after addition of the buffer. Beads
669 were collected by centrifugation and once briefly washed with 200 µl of interaction buffer. 50 µl
670 of interaction buffer with 1 µg/µl 3xFlag peptide was added to the beads and samples were
671 incubated rotating at 4 °C for 1.5 hours to elute proteins from the beads. Samples were
672 subsequently analyzed by SDS-PAGE and Coomassie staining.
673

674 ***In vitro* phosphorylation and dephosphorylation of Ipl1/Sli15**

675 Recombinant Ipl1/Sli15 was diluted in interaction buffer (25 mM HEPES pH 7.4, 200 mM NaCl,
676 1 mM $MgCl_2$, 2.5 % (v/v) glycerol, 0.01 % (v/v) Tween-20) supplemented with 1 mM $MnCl_2$. λ-
677 Protein Phosphatase (NEB) or 500 µM ATP was added and samples were incubated at 30 °C
678 for 30 minutes.
679

680 ***In vitro* kinase assay**

681 *In vitro* kinase reactions were prepared in a total reaction volume of 90 µl. Recombinant KMN,
682 Ipl1/Sli15 or a mixture of KMN and Ipl1/Sli15 were diluted in kinase buffer (20 mM HEPES
683 pH 7.4, 100 mM KCl, 10 mM $MgCl_2$, 10 mM $MnCl_2$, 25 mM β-glycerol phosphate, 1 mM DTT)
684 supplemented with 100 µM cold ATP and 83.25 nM hot ^{32}P-γ-ATP (Hartmann Analytic).
685 Samples were incubated at 30 °C and 20 µl aliquots were taken after 0, 5, 15 and 30 minutes.
686 Reactions were stopped by addition of 6x SDS-PAGE loading buffer, boiled at 95 °C and
687 analyzed by SDS-PAGE. Gels were stained with Coomassie dried afterwards. ^{32}P

688 autoradiography was detected with a FLA-3000 Imaging Scanner (Fujifilm).
689

690 **Purification of recombinant Ipl1/Sli15 from *E. coli***

691 Ipl1/6xHis-Sli15 was expressed in BL21 *E. coli* cells. 4 L TB medium with 50 µg/ml kanamycin
692 were inoculated with 100 ml of a saturated overnight culture. Cells were incubated at 37 °C,
693 shaking at 180 rpm, until an $OD_{600} \approx 0.7$ was reached. Expression of Ipl1/Sli15 was induced
694 by addition of 0.4 mM IPTG. Cells were further incubated for 3 h and afterwards harvested by
695 centrifugation, washed in PBS and stored at -80 °C until further processing.
696 Cells were resuspended in 90 ml lysis buffer (50 mM Na_2HPO_4/NaH_2PO_4 pH 8.0, 300 mM
697 NaCl, 5 % (v/v) glycerol, 20 mM imidazole, 0.5 mM TCEP) supplemented with Pierce™
698 Protease Inhibitor (EDTA-free; ThermoFisher Scientific) and 1 mM PMSF and lysed by
699 sonication. The lysate was cleared by centrifugation and loaded onto two serially connected
700 HisTrap 5 ml columns (Cytiva) which were connected to a ÄKTA FPLC system (GE
701 Healthcare). Columns were washed with lysis buffer and bound proteins were eluted with a
702 linear imidazole gradient (20 – 500 mM). Elution fractions were collected and analyzed by
703 SDS-PAGE. Fractions of comparable quality were pooled, concentrated to approximately
704 500 µl and subjected to size exclusion chromatography using Superdex 200 10/300 GL
705 column (GE Healthcare; 20 mM HEPES pH 7.4, 250 mM NaCl, 1 mM $MgCl_2$, 5 % (v/v)
706 glycerol, 0.5 mM TCEP). Elution fractions were analyzed by SDS-PAGE and comparable
707 samples were pooled, aliquoted, snap-frozen in liquid N_2 and stored at -80 °C.
708

709 **In vivo biotinylation and affinity purification with TurboID**

710 Cell extracts from the respective yeast strains were prepared from log-phase cultures. Cells
711 were lysed by bead-beating (BioSpec) in Lysis buffer (20 mM Hepes pH 7.4, 200 mM NaCl,
712 1 mM $MgCl_2$, 0.5 mM TCEP, 2.5 % glycerol. After centrifugation, 500 µl cleared lysate was
713 incubated with 50 µl pre-equilibrated streptavidin-sepharose beads (Cytiva) with rotation at
714 4°C overnight. Beads were washed twice with wash buffer (Lysis buffer + 0.05 % (v/v) TX-100),
715 twice with wash buffer + 2 % (w/v) SDS, twice with wash buffer + 0.1 % (w/v) SDS and finally
716 twice with wash buffer. Proteins were eluted off the beads with SDS-PAGE loading buffer and
717 analyzed by western blotting.
718

719 **Pt/C low angle rotary shadowing electron microscopy**

720 The peak elution fractions from gel filtrations of recombinant KMN complexes were further
721 prepared for rotary shadowing EM analysis by diluting the complexes to ~70 µg/ml in spraying
722 buffer, containing 100 mM ammonium acetate and 30 % (v/v) glycerol, pH adjusted to 7.4. After
723 dilution, the samples were sprayed onto freshly cleaved mica chips and immediately

transferred into a Bal-Tec MED020 high vacuum evaporator equipped with electron guns. After drying in the vacuum, the rotating samples were coated with 0.5 nm platinum at an elevation angle between 5° and 6°, followed by 7 nm carbon at 90°. The produced replicas were floated off from the mica chips and picked up on 400mesh Cu/Pd grids. The grids were inspected in an FEI Morgagni 268D TEM operated at 80kV. Electron micrographs were acquired using an 11 megapixel Morada CCD camera from Olympus-SIS. Fiji was used for image analysis.

Chemical crosslinking and mass spectrometry

50-60 µg of recombinant protein complexes were crosslinked with 1:1 isotopically-labeled (d_0/d_{12}) BS3 (Bis[sulfosuccinimidyl] suberate, Creative molecules) in a Thermomixer at 35°C for 30 min at 1200 rpm. The reaction was quenched with 100 mM ammonium bicarbonate for 5 minutes at room temperature and supplemented with 8 M urea to a final concentration of 6 M. After reduction and alkylation crosslinked proteins were digested with Lys-C (1:50 w/w, Wako) for 3 hours, diluted with 50 mM ammonium bicarbonate to 1 M urea and digested with trypsin (1:50 w/w, Promega) overnight. Crosslinked peptides were purified by reversed phase chromatography using C18 cartridges (Sep-Pak, Waters). Crosslinked peptides were enriched by peptide size exclusion chromatography and analyzed by tandem mass spectrometry (Orbitrap Elite, Thermo Scientific). Fragment ion spectra were searched and crosslinks identified by the dedicated software program xQuest.

Acknowledgements

This work was funded by the Deutsche Forschungsgemeinschaft (DFG, German Research Foundation) – SFB1430 – Project-ID 424228829. Microscopy experiments were carried out with support from the Imaging Center Campus Essen Core Facility (ICCE). The DeltaVision Elite high resolution microscope was obtained through Deutsche Forschungsgemeinschaft funding (Major Research Instrumentation Program as per Art. 91b GG, INST 20876/275-1). The laboratory of F.H. was supported by the European Research Council (ERC)-StG (638218) and by the GFF NÖ (Endowed Professorship, Province of Lower Austria).

Author contributions

A.D. conducted and analyzed the majority of experiments, supported by J.S. and F.H.; S.T. performed *in vivo* biotinylation experiments, K.J. supported strain and plasmid construction; I.R.V. performed and analyzed structure predictions. F.H., S.S. and J.F. contributed and analyzed XL-MS experiments; A.D. and S.W. designed the study and wrote the manuscript.

759 **Conflict of interest**

760 The authors declare that they have no conflict of interests.

761

762

763 **Main Figure Legends**

764 **Figure 1: Mutation of the Kre28 helical bundle renders yeast cells inviable in the**
765 **presence of benomyl**

766 A: AlphaFold2 structure prediction of the Spc105$^{490-917}$/Kre28 heterodimer. The unstructured
767 N-terminal half of Spc105 was omitted form the structure prediction. Functionally relevant
768 regions of the proteins such as Zwint or RWD domains are labelled in distinct colors.

769 B: Secondary structure prediction of *S. cerevisiae* Zwint (top), *H. sapiens* Zwint (bottom) and
770 multiple sequence alignment of the so called Zwint helix of related eukaryotic proteins (middle).
771 Functional regions of Kre28 required for Spc105 (Roy *et al*, 2022), Mtw1c binding
772 (Ghodgaonkar-Steger *et al*, 2020), the C-terminal RWD domain (Tromer *et al*, 2019) and the
773 newly identified Zwint helix are marked.

774 C: Representative images of dissection plates of diploid heterozygous Kre28/Kre28-6xFlag
775 yeast strains with different 6xFlag-tagged alleles (WT, *ΔZwint*, *ΔRWD* or *ΔZwint ΔRWD*).
776 Strains were sporulated and dissected and the plates were incubated at 30 °C for three days.
777 Spores were subsequently analyzed regarding their genotype. While haploid strains with single
778 deletion of either the Zwint helix or the RWD domain are viable, simultaneous deletion of both
779 domains does not support viability of haploid yeasts.

780 D: Western blot analysis to compare protein expression levels of Kre28^{WT}, *kre28$^{\Delta Zwint}$* and
781 *kre28$^{\Delta RWD}$* in haploid yeast strains. Pgk1 was used as loading control.

782 E: Serial dilution assay of haploid yeast strains with different Kre28 alleles. Strains with the
783 indicated genotypes were serially diluted, spotted on YEPD or YEPD + benomyl plates and
784 incubated at the indicated temperatures. A *mad1*Δ strain was used as control for benomyl
785 hypersensitivity.

786

787 **Figure 2: The Kre28 helical bundle mutant displays defects in tension-dependent error-**
788 **correction**

789 A: Analysis of cell cycle progression. Haploid yeast strains with either Kre28^{WT}, *kre28$^{\Delta Zwint}$* or
790 *mad1*Δ were first arrested in G1 using α factor and then released into medium containing
791 nocodazole to depolymerize microtubules and test for functionality of the spindle assembly
792 checkpoint. Samples for western blot analysis were collected every 30 minutes and were
793 analyzed for Pds1 levels as readout for mitotic progression. A *mad1*Δ strain was used as
794 positive control for spindle assembly checkpoint deficiency.

795 B: Serial dilution assay of haploid yeast strains with Kre28^{WT} or *kre28$^{\Delta Zwint}$* in a *MAD1* or *mad1*Δ
796 strain background. Strains with the indicated genotypes were serially diluted, spotted on YEPD
797 or YEPD + benomyl plates and incubated at the indicated temperatures.

798 C: Analysis of cell cycle progression after release from a nocodazole arrest. Kre28^{WT} or

799 *kre28$^{\Delta Zwint}$* cells were arrested in mitosis using nocodazole and released into medium with
800 alpha factor to arrest cells in the next G1 phase. Samples were collected every 15 minutes
801 and Pds1 levels as marker for mitotic progression were analyzed by western blot. Pgk1 served
802 as loading control.
803 D and E: Analysis of segregation of fluorescently labelled chromosome XII by live cell
804 microscopy. Kre28^{WT} and *kre28$^{\Delta Zwint}$* cells with fluorescently labelled chromosome XII (CEN12-
805 GFP) and spindle pole bodies (Spc42-mCherry) were released from a nocodazole arrest and
806 segregation of chromosome XII during the next anaphase was followed. Representative
807 images of segregation and missegregation are shown in D, a quantification of the
808 missegregation rate is shown in E. Data is derived from three independent experiments
809 analyzing n > 100 cells per condition. The dots represent the data of each individual
810 experiment. p value was calculated by an unpaired t-test.
811 F: Representative images of dissection plates of diploid heterozygous Kre28/Kre28-6xFlag
812 Ipl1/*ipl1-1* strains. Strains were sporulated and dissected and the plates were incubated at
813 30 °C for three days. Afterwards, the spores were analyzed regarding their genotype. Haploid
814 strains with both *kre28$^{\Delta Zwint}$* and *ipl1-1* are viable but display severe growth retardation.
815 G: Summary of genetic interactions between the *kre28$^{\Delta Zwint}$* allele and mutant alleles of outer
816 kinetochore subunits (*ndc80-1*, *duo1$^{\Delta SxIP}$*, *dam1-1* and *dam1-9*), the Ndc80c recruiter Cnn1
817 (*cnn1Δ*), CPC subunits (*ipl1-1*, *sli15-3*), CPC recruiters (*sgo1Δ*, *ctf19$^{\Delta C\text{-}RWD}$*) or a spindle
818 assembly checkpoint component (*mad1Δ*).
819

820 **Figure 3: The Kre28$^{\Delta Zwint}$ mutant reduces the level of Spc105/Kre28 at kinetochore**
821 **clusters *in vivo***
822 A and B: Live cell imaging of yeast cells with GFP-tagged KMN subunits. Representative
823 images of metaphase and anaphase cells are shown on the left, quantification of fluorescence
824 signal intensities on the right. Kinetochore recruitment of Mtw1-GFP (Mtw1 complex), Nuf2-
825 GFP (Ndc80 complex) and Spc105-GFP was analyzed in Kre28^{WT} and *kre28$^{\Delta Zwint}$* strain
826 backgrounds. In addition, signal intensities of GFP-Kre28^{WT} or GFP-*kre28$^{\Delta Zwint}$* were quantified.
827 The C-terminus of Spc42 was fused to RFP to label the position of the mitotic spindle. The
828 mean of metaphase signal intensities in the wildtype strain was defined as 1 and all other data
829 was normalized to this value. Means +/- standard deviation are plotted. p values were
830 calculated with a Kruskal-Wallis test. n > 100 kinetochore clusters were analyzed for each
831 condition. Representative data from at least two independent experiments is shown.
832 C: *In vitro* analysis of KMN stability with Kre28^{WT} or Kre28$^{\Delta Zwint}$ subunits. KMN with either
833 Kre28^{WT} or Kre28$^{\Delta Zwint}$ was immobilized on M2 anti-Flag beads using a Flag tag at the C-
834 terminus of Spc105 and buffer was added to the beads for dilution. Samples were taken at the

835 indicated time points to follow dissociation of Mtw1c and Ndc80c from Spc105/Kre28 over time.
836 Proteins were eluted from the beads using 3xFlag peptide and the eluate was analyzed by
837 SDS-PAGE and Coomassie staining.
838 D: Quantification of indicated subunits by band intensity in Kre28 wildtype or mutant
839 complexes.
840

841 **Figure 4: Ipl1/Sli15 binds to KMN via the Spc105/Kre28 subcomplex *in vitro***
842 A: Single-step isolation of a recombinant budding yeast KMN network from Sf9 insect cells.
843 Left side shows Coomassie-stained SDS-PAGE of anti-Flag purification of Spc105-Flag. Right
844 panel shows consecutive fractions from size exclusion chromatography on a Superose 6
845 column.
846 B: Gallery of electron micrographs showing recombinant KMN network visualized by Pt/C
847 rotary shadowing EM. Distinct configurations are shown in which the end of the Ndc80 complex
848 shows one or more appendages.
849 C: Pull down assays to test for binding of Ipl1/Sli15 to KMN. KMN containing either Kre28^{WT} or
850 Kre28$^{\Delta Zwint}$ was purified from Sf9 insect cells and immobilized on M2 anti-Flag beads.
851 Recombinant Ipl1/Sli15 was added to test for its binding to KMN. Proteins were eluted from
852 beads by addition of 3xFlag peptide. Input and pull down samples were analyzed by SDS-
853 PAGE and Coomassie staining or western blot to detect 6xHis-tagged Sli15.
854 D: Pull down assay to test for binding of Ipl1/Sli15 to Spc105/Kre28 or Mtw1c/Ndc80c. Either
855 Spc105/Kre28 or Mtw1c in combination with Ndc80c were purified from Sf9 insect cells and
856 immobilized on M2 anti-Flag beads. Recombinant Ipl1/Sli15 was added to test for its binding
857 to the immobilized proteins. Proteins bound to the beads were finally eluted with 3xFlag peptide
858 and input and pull down samples were analyzed by SDS-PAGE followed by Coomassie
859 staining or western blot to detect 6xHis-tagged Sli15.
860 E: Pull down assay to analyze the impact of Ipl1/Sli15 phosphorylation on binding to
861 Spc105/Kre28. Spc105/Kre28 was purified from Sf9 insect cells and immobilized on M2 anti-
862 Flag beads. Prior to addition to the loaded beads, recombinant Ipl1/Sli15 was *in vitro*
863 autophosphorylated (+ATP), dephosphorylated by λ phosphatase or left untreated. After
864 incubation with the immobilized Spc105/Kre28, bound proteins were eluted from the beads
865 using 3xFlag peptide and input and pull down samples were analyzed by SDS-PAGE and
866 Coomassie staining or western blot to detect 6xHis-Sli15. The mobility of Ipl1 and Sli15 during
867 SDS-PAGE depends on their phosphorylation status. LC and HC mark the light and heavy
868 chains of the M2 anti-Flag antibody. F: *In vivo* proximity-biotinylation experiment using Spc105-
869 TurboID and different Flag-tagged potential interactors. Yeast lysates were prepared from the
870 indicated strains and subjected to a Streptavidin affinity purification to isolate biotinylated
871 proteins. Note that Kre28 and Sli15 are only detected in pull downs from strains that also

872 express Spc105-TurboID. The major endogenously biotinylated proteins Acc1, Pyc1/2 or Arc1
873 enriched in in the Streptavidin pull down are indicated.
874

875 **Figure 5: Chemical cross-linking mass spectrometry analysis of the KMN-Ipl1/Sli15**
876 **assembly**
877 A: Schematic illustration of Sli15 and Ipl1. Sli15 associates with its N-terminal CEN box to
878 Bir1/Survivin and Nbl1/Borealin. The C-terminal IN box binds to the globular kinase domain of
879 Ipl1.
880 B: Network diagram of inter- and intramolecular Lys-Lys crosslinks of a KMN-Ipl1/Sli15
881 assembly. Recombinant KMN and Ipl1/Sli15 were mixed at equimolar amounts and incubated
882 in the presence of BS3. Functional domains of Ipl1 and Sli15 are indicated in the legend.
883 Interlinks originating from Sli15 or Ipl1 to KMN subunits are highlighted.
884

885 **Figure 6: Artificial recruitment of Sli15 to Mtw1 suppresses the *kre28$^{\Delta Zwint}$* mutant**
886 **phenotype**
887 A: Illustration of artificial recruitment of Ipl1 to KMN by fusion of a C-terminal fragment of Sli15
888 to the C-terminus of Mtw1 and schematic of the architecture of two different Mtw1-Sli15 fusion
889 proteins. Two C-terminal fragments of Sli15 were fused to the C-terminus of Mtw1, separated
890 by a 6xHA tag. Ipl1 is recruited to the fusion proteins by binding to the IN box of Sli15. The red
891 asterisks mark the position of W646G and F680A amino acid substitutions which prevent
892 binding of Ipl1 to Sli15. The genes encoding the fusion constructs were integrated at the *LYS2*
893 locus and under control of the Mtw1 promotor.
894 B: Western blot analysis of Mtw1 fusion proteins and Kre28 mutants. Extracts of indicated
895 strains were blotted for the presence of fusion proteins (anti-HA), Kre28 wildtype or mutant
896 (anti-Flag).
897 C: Serial dilution assay with haploid yeast strains with Kre28^{WT} or *kre28$^{\Delta Zwint}$* expressing
898 different Mtw1-Sli15 fusion proteins. Serial dilutions of yeast strains with the indicated
899 genotypes were spotted on YEPD and YEPD + benomyl plates and incubated at the indicated
900 temperatures.
901 D: Scoring of chromosome segregation in Kre28^{WT} or *kre28$^{\Delta Zwint}$* with fluorescently labelled
902 chromosome XII (CEN12-GFP) and spindle pole bodies (Spc42-mCherry) expressing different
903 Mtw1-Sli15 fusion proteins. Cells were released from a nocodazole arrest and segregation of
904 chromosome XII in the first anaphase after release was analyzed. Missegregation rates in the
905 different strains are displayed with data from three independent experiments. Mean values +/-
906 standard deviation are plotted. The dots represent the data from three individual experiments.
907 n > 110 cells were analyzed for each condition in each experiment. p values were calculated

908 with an unpaired t-test.

909

910 **Figure 7: The N-terminus of Ipl1 is implicated in outer kinetochore recruitment**

911 A: Multiple sequence alignment of the Ipl1 N-terminal domain from different yeast species.
912 MSA was generated in Jalview and colored according to ClustalW scheme. Position of
913 residues mutated in the *ipl1*^{3A} mutant is indicated. Abbreviations as follows: S.c.
914 Saccharomyces cerevisiae; S.b. Saccharomyces boulardii; K.b. Kazachstania barnetii; Z.b.
915 Zygosaccharomyces parabailii; Z.r. Zygosaccharomyces rouxii; A.g. Ashbya gossypii; E.s.
916 Eromethecium sinecaudum; K.l. Kluyeromyces lactis; K.m. Kluyveromyces marxianis.

917 B: Alphafold2 structure prediction of a KMN network with Mtw1 complex (green), Spc24/Spc25
918 (grey), Spc105/Kre (red and blue) and the N-terminal 30-residue segment of Ipl1 (turquoise).
919 Insert shows magnified view of a predicted binding interface formed between the
920 Spc105/Kre28 helical bundle and the Ipl1 N-terminus.

921 C: Pull down assay with recombinant Spc105/Kre28 and Sli15/Ipl1 wildtype or Ipl1 L11A, R23A,
922 I29A point mutant. After incubation with the immobilized Spc105/Kre28, bound proteins were
923 eluted from the beads using 3xFlag peptide and input and pull down samples were analyzed
924 by SDS-PAGE and Coomassie staining or western blot to detect 6xHis-Sli15. 6xHis-Sli15
925 signals were quantified in the pull down and normalized to the wildtype.

926 D: Testing synthetic genetic effects between different Ipl1 recruitment mechanisms. The *sgo1-*
927 *aid* or ctf19$^{\Delta RWD\text{-}C}$ alleles compromise centromere-dependent recruitment pathways, but are
928 compatible with viability.

929 E: Serial dilution assay of Sgo1-aid strains in different Ipl1 wildtype or mutant backgrounds.
930 Depletion of Sgo1-aid is induced in the presence of Galactose and NAA.

931 F: Serial dilution assays of IPL1 wildtype or mutant strains in either a CTF19 wildtype or a
932 ctf19$^{\Delta RWD\text{-}C}$ genetic background. Strains were incubated on YEPD plates. Note that Ipl1 point
933 or deletion mutants compromise viability under conditions when Sgo1 is depleted.

934 G: Serial dilution assays of IPL1 wildtype or mutant strains in either a CTF19 wildtype or a
935 *ctf19*$^{\Delta RWD\text{-}C}$ genetic background. Strains were incubated on YEPD plates containing benomyl.

936

937 **Figure 8: A model for conformation-sensitive docking of Ipl1 to the outer kinetochore**

938 A: Organization of centromere-binding modules and outer kinetochore docking sites in the
939 Ipl1/Sli15 complex.

940 B: Model for how conformation-sensitive outer kinetochore docking could contribute to tension-
941 dependent error correction. To improve clarity, only Ipl1 and the IN box of Sli15 is depicted.
942 Other Sli15 segments may provide additional interactions with inner and outer kinetochore.

943 **Figure Supplement Legends**

944 **Figure 1 – Supplement 1: Additional information on the Spc105/Kre28 structure**
945 **prediction**

946 A: Predicted alignment error of the Spc105$^{490-917}$/Kre28 structure prediction.

947 B: Predicted structure of Spc105$^{490-917}$/Kre28 colored by local pLDDT confidence score.

948

949 **Figure 1 – Supplement 2: Detailed mutagenesis analysis of the Zwint helix**

950 A: Multiple sequence alignment of Kre28 sequences from different yeast species. Conserved
951 residues are colored according to the Clustal color scheme. Positions of smaller Zwint helix
952 deletions and alanine substitutions of conserved residues are marked.

953 B: Western blot analysis of different Kre28/Zwint deletion or point mutants. Extracts of log
954 phase yeast cells were analyzed, Pgk1 blot serves as a loading control.

955 C and D: Serial dilution assays of haploid yeast strains with different Kre28 Zwint helix
956 deletions or point mutations of conserved residues. Strains with the indicated genotypes were
957 serially diluted and spotted on YEPD or YEPD + benomyl plates and incubated at the indicated
958 temperatures.

959

960 **Figure 2 – Supplement: Viability assay after nocodazole treatment**

961 Kre28^{WT}, *kre28*$^{\Delta Zwint}$ and *mad1*Δ cells were treated with nocodazole for 2 hours. Before and
962 after treatment, a defined number of cells was plated on YEPD plates and incubated at 30 °C.
963 After two days, the number of colonies was counted. Images of the plates are shown on the
964 left, the quantification of colony formation in the right. For each strain, the number of colonies
965 of the untreated samples was defined as 100 %.

966

967 **Figure 3 – Supplement: Western blot analysis of GFP-tagged KMN subunits and live cell**
968 **microscopy of Sgo1-GFP**

969 A: Western blot analysis to compare the expression of different GFP-tagged KMN subunits. in
970 Kre28 wildtype and mutant cells. Pgk1 served as loading control.

971 B: Western blot analysis of expression level of N-terminal GFP-tagged Kre28 in wildtype and
972 mutant form.

973 C: Western blot analysis of C-terminal GFP-tagged Kre28 in wildtype and mutant form.

974 D: Quantification of Kre28-GFP fluorescence signals at metaphase and anaphase
975 kinetochores. Strains with either Kre28^{WT}-GFP or *kre28*$^{\Delta Zwint}$-GFP were analyzed by live cell
976 microscopy. The C-terminus of Spc42 was fused to RFP to label the position of the mitotic
977 spindle. The mean of metaphase signal intensities in the wildtype strain was defined as 1 and
978 all other data was normalized to this value. Means +/- standard deviation are plotted. p values

979 were calculated with a Kruskal-Wallis test. n > 100 kinetochore clusters were analyzed for each
980 condition. Representative data from two independent experiments is shown.
981 E: Live cell microscopy for analysis of Sgo1-GFP kinetochore localization in a Kre28^{WT} or
982 *kre28$^{\Delta Zwint}$* strain background. Representative images of a metaphase and an anaphase cell
983 are shown on the left and quantification of Sgo1-GFP signals in cells with short mitotic spindles
984 is shown on the right. Data was normalized to the mean value measured for the Kre28^{WT} strain.
985 Mean values +/- standard deviation are plotted. A Mann-Whitney test was used to test for
986 statistical significance.
987

988 **Figure 4 – Supplement 1: *In vitro* dephosphorylation of Ipl1/Sli15 and gel filtration**
989 **analysis**
990 A: *In vitro* dephosphorylation of Ipl1/Sli15. Recombinant Ipl1/Sli15 was treated with λ
991 phosphatase for 30 minutes at 30 °C. Untreated and dephosphorylated Ipl1/Sli15 were
992 analyzed by SDS-PAGE and Coomassie staining. Both Ipl1 and Sli15 show faster migration
993 after phosphatase treatment.
994 B: Gelfiltration analysis of recombinant Ipl1/Sl15 complex on a Superdex 200 column. Input
995 and consecutive fractions from size exclusion chromatography are loaded on SDS-PAGE and
996 stained with Coomassie. Note that the truncated Sli15 fragment purifies away from the
997 Ipl1/Sli15 complex.
998

999 **Figure 4 – Supplement 2: Pull -down experiment and *in vitro* kinase reaction with**
1000 **Ipl1/Sli15 and KMN**
1001 A: Pull down assays to analyze binding of Ipl1/Sli15 to KMN. KMN with either Kre28^{WT} or
1002 Kre28$^{\Delta Zwint}$ was purified from Sf9 cells and immobilized on M2 anti-Flag beads. Loaded beads
1003 were incubated with buffer or recombinant Ipl1/Sli15, afterwards proteins bound to the beads
1004 were eluted with 3xFlag peptide. Input and pull down samples were analyzed by SDS-PAGE
1005 and Coomassie staining or western blot to detect 6xHis-tagged Sli15.
1006 B: *In vitro* kinase reaction with Ipl1/Sli15 or Ipl1/Sli15 in presence of recombinant KMN
1007 analyzed over time. Coomassie stained gel at the top, corresponding autoradiograph at the
1008 bottom. For control a KMN only sample taken 30 min after in incubation with radioactive ATP
1009 is shown at the in first lane. C: Quantification phosphorylated Ipl1 signal over time alone (blue
1010 curve) or in presence of KMN (green curve).
1011

1012 **Figure 6 – Supplement: Western blot analysis of different Mtw1-Sli15 fusion proteins**
1013 Western blot analysis comparing the expression of Mtw1-6xHA-Sli15 fusion proteins (shorter
1014 Fusion I and longer Fusion II) in wild-type form or in mutant form preventing Ipl1 binding. The

respective strains were used for serial dilution assays shown in Figure 6B. Pgk1 served as loading control.

Figure 7 – Supplement 1: **A.** pLDDT scores of the “spliced” model of Mtw1c-Spc24/25-Spc105/Kre28/Ipl1 1-30 complex (left) and the separate prediction for Spc105 residues 421-917, Kre28, and Ipl1 residues 1-30 (right). **B.** PAE scores for the “spliced” model for all 10 AF2 predictions. Fragment boundaries are indicated by black lines, blue are favourable scores, red are unfavourable.

Figure 7 - Supplement 2: **A**. Ipl1 1-30 binding site in AF2 predictions of the “SKI” complex: **Top row**: All 10 predicted models, with potentially interacting side chains shown as green sticks **Middle row**: Highest ranking model **Bottom row**: pLDDT scores for highest ranking model. The Spc105/Kre28 surface is colored by electrostatic potential. **B.** PAE scores for the “SKI” model for all 10 AF2 predictions. Fragment boundaries are indicated by black lines, blue are favourable scores, red are unfavourable.

References

1. Yatskevich, S., Muir, K.W., Bellini, D., Zhang, Z., Yang, J., Tischer, T., Predin, M., Dendooven, T., McLaughlin, S.H., and Barford, D. (2022). Structure of the human inner kinetochore bound to a centromeric CENP-A nucleosome. Science *376*, 844-852. 10.1126/science.abn3810.
2. Dendooven, T., Zhang, Z., Yang, J., McLaughlin, S.H., Schwab, J., Scheres, S.H.W., Yatskevich, S., and Barford, D. (2023). Cryo-EM structure of the complete inner kinetochore of the budding yeast point centromere. Science Advances *9*, eadg7480. 10.1126/sciadv.adg7480.
3. Pesenti, M.E., Raisch, T., Conti, D., Walstein, K., Hoffmann, I., Vogt, D., Prumbaum, D., Vetter, I.R., Raunser, S., and Musacchio, A. (2022). Structure of the human inner kinetochore CCAN complex and its significance for human centromere organization. Molecular Cell *82*, 2113-2131.e2118. 10.1016/j.molcel.2022.04.027.
4. Xiao, H., Wang, F., Wisniewski, J., Shaytan, A.K., Ghirlando, R., FitzGerald, P.C., Huang, Y., Wei, D., Li, S., Landsman, D., et al. (2017). Molecular basis of CENP-C association with the CENP-A nucleosome at yeast centromeres. Genes Dev. *31*, 1958-1972. 10.1101/gad.304782.117.
5. Kato, H., Jiang, J., Zhou, B.-R., Rozendaal, M., Feng, H., Ghirlando, R., Xiao, T.S., Straight, A.F., and Bai, Y. (2013). A Conserved Mechanism for Centromeric Nucleosome Recognition by Centromere Protein CENP-C. Science *340*, 1110-1113. 10.1126/science.1235532.
6. Polley, S., Raisch, T., Ghetti, S., Korner, M., Terbeck, M., Grater, F., Raunser, S., Aponte-Santamaria, C., Vetter, I.R., and Musacchio, A. (2024). Structure of the human KMN complex and implications for regulation of its assembly. Nat Struct Mol Biol *31*, 861-873. 10.1038/s41594-024-01230-9.
7. Yatskevich, S., Yang, J., Bellini, D., Zhang, Z., and Barford, D. (2024). Structure of the human outer kinetochore KMN network complex. Nat Struct Mol Biol *31*, 874-883. 10.1038/s41594-024-01249-y.
8. Dimitrova, Y.N., Jenni, S., Valverde, R., Khin, Y., and Harrison, S.C. (2016). Structure of the MIND Complex Defines a Regulatory Focus for Yeast Kinetochore Assembly. Cell *167*, 1014-1027 e1012. 10.1016/j.cell.2016.10.011.
9. Weir, J.R., Faesen, A.C., Klare, K., Petrovic, A., Basilico, F., Fischböck, J., Pentakota, S., Keller, J., Pesenti, M.E., Pan, D., et al. (2016). Insights from biochemical reconstitution into the architecture of human kinetochores. Nature *537*, 249-253. 10.1038/nature19333.
10. Petrovic, A., Keller, J., Liu, Y., Overlack, K., John, J., Dimitrova, Y.N., Jenni, S., van Gerwen, S., Stege, P., Wohlgemuth, S., et al. (2016). Structure of the MIS12 Complex and Molecular Basis of Its Interaction with CENP-C at Human Kinetochores. Cell *167*, 1028-1040.e1015. 10.1016/j.cell.2016.10.005.
11. Hornung, P., Troc, P., Malvezzi, F., Maier, M., Demianova, Z., Zimniak, T., Litos, G., Lampert, F., Schleiffer, A., Brunner, M., et al. (2014). A cooperative mechanism drives budding yeast kinetochore assembly downstream of CENP-A. Journal of Cell Biology *206*, 509-524. 10.1083/jcb.201403081.
12. Musacchio, A., and Desai, A. (2017). A Molecular View of Kinetochore Assembly and Function. Biology (Basel) *6*, 5. 10.3390/biology6010005.
13. Ciferri, C., Pasqualato, S., Screpanti, E., Varetti, G., Santaguida, S., Dos Reis, G., Maiolica, A., Polka, J., De Luca, J.G., De Wulf, P., et al. (2008). Implications for Kinetochore-Microtubule Attachment from the Structure of an Engineered Ndc80 Complex. Cell *133*, 427-439. 10.1016/j.cell.2008.03.020.
14. Wei, R.R., Al-Bassam, J., and Harrison, S.C. (2007). The Ndc80/HEC1 complex is a contact point for kinetochore-microtubule attachment. Nat. Struct. Mol. Biol. *14*, 54-59. 10.1038/nsmb1186.
15. Wilson-Kubalek, E.M., Cheeseman, I.M., Yoshioka, C., Desai, A., and Milligan, R.A. (2008). Orientation and structure of the Ndc80 complex on the microtubule lattice. Journal of Cell Biology *182*, 1055-1061. 10.1083/jcb.200804170.
16. Pleuger, R., Cozma, C., Hohoff, S., Denkhaus, C., Dudziak, A., Kaschani, F., Kaiser, M., Musacchio, A., Vetter, I.R., and Westermann, S. (2024). Microtubule end-on attachment maturation

regulates Mps1 association with its kinetochore receptor. Curr Biol *34*, 2279-2293 e2276. 10.1016/j.cub.2024.03.062.

17. Parnell, E.J., Jenson, E.E., and Miller, M.P. (2024). A conserved site on Ndc80 complex facilitates dynamic recruitment of Mps1 to yeast kinetochores to promote accurate chromosome segregation. Curr Biol *34*, 2294-2307 e2294. 10.1016/j.cub.2024.04.054.
18. Zahm, J.A., and Harrison, S.C. (2024). A communication hub for phosphoregulation of kinetochore-microtubule attachment. Curr Biol *34*, 2308-2318 e2306. 10.1016/j.cub.2024.04.067.
19. Malvezzi, F., Litos, G., Schleiffer, A., Heuck, A., Mechtler, K., Clausen, T., and Westermann, S. (2013). A structural basis for kinetochore recruitment of the Ndc80 complex via two distinct centromere receptors. EMBO J *32*, 409-423. emboj2012356 [pii]

10.1038/emboj.2012.356.

20. Petrovic, A., Mosalaganti, S., Keller, J., Mattiuzzo, M., Overlack, K., Krenn, V., De Antoni, A., Wohlgemuth, S., Cecatiello, V., Pasqualato, S., et al. (2014). Modular Assembly of RWD Domains on the Mis12 Complex Underlies Outer Kinetochore Organization. Molecular Cell *53*, 591-605. 10.1016/j.molcel.2014.01.019.
21. Ghodgaonkar-Steger, M., Potocnjak, M., Zimniak, T., Fischbock-Halwachs, J., Solis-Mezarino, V., Singh, S., Speljko, T., Hagemann, G., Drexler, D.J., Witte, G., and Herzog, F. (2020). C-Terminal Motifs of the MTW1 Complex Cooperatively Stabilize Outer Kinetochore Assembly in Budding Yeast. Cell Rep *32*, 108190. 10.1016/j.celrep.2020.108190.
22. Roy, B., Sim, J., Han, S.J.Y., and Joglekar, A.P. (2022). Kre28–Spc105 interaction is essential for Spc105 loading at the kinetochore. Open Biology *12*, 210274. 10.1098/rsob.210274.
23. London, N., Ceto, S., Ranish, J.A., and Biggins, S. (2012). Phosphoregulation of Spc105 by Mps1 and PP1 Regulates Bub1 Localization to Kinetochores. Current Biology *22*, 900-906. 10.1016/j.cub.2012.03.052.
24. Shepperd, L.A., Meadows, J.C., Sochaj, A.M., Lancaster, T.C., Zou, J., Buttrick, G.J., Rappsilber, J., Hardwick, K.G., and Millar, J.B.A. (2012). Phosphodependent Recruitment of Bub1 and Bub3 to Spc7/KNL1 by Mph1 Kinase Maintains the Spindle Checkpoint. Current Biology *22*, 891-899. 10.1016/j.cub.2012.03.051.
25. Yamagishi, Y., Yang, C.-H., Tanno, Y., and Watanabe, Y. (2012). MPS1/Mph1 phosphorylates the kinetochore protein KNL1/Spc7 to recruit SAC components. Nature Cell Biology *14*, 746-752. 10.1038/ncb2515.
26. Rosenberg, J.S., Cross, F.R., and Funabiki, H. (2011). KNL1/Spc105 Recruits PP1 to Silence the Spindle Assembly Checkpoint. Current Biology *21*, 942-947. 10.1016/j.cub.2011.04.011.
27. Nijenhuis, W., Vallardi, G., Teixeira, A., Kops, G.J.P.L., and Saurin, A.T. (2014). Negative feedback at kinetochores underlies a responsive spindle checkpoint signal. Nature Cell Biology *16*, 1257-1264. 10.1038/ncb3065.
28. Meadows, J.C., Shepperd, L.A., Vanoosthuyse, V., Lancaster, T.C., Sochaj, A.M., Buttrick, G.J., Hardwick, K.G., and Millar, J.B.A. (2011). Spindle Checkpoint Silencing Requires Association of PP1 to Both Spc7 and Kinesin-8 Motors. Developmental Cell *20*, 739-750. 10.1016/j.devcel.2011.05.008.
29. Pagliuca, C., Draviam, V.M., Marco, E., Sorger, P.K., and Wulf, P.D. (2009). Roles for the Conserved Spc105p/Kre28p Complex in Kinetochore-Microtubule Binding and the Spindle Assembly Checkpoint. PLOS ONE *4*, e7640. 10.1371/journal.pone.0007640.
30. Tromer, E.C., van Hooff, J.J.E., Kops, G.J.P.L., and Snel, B. (2019). Mosaic origin of the eukaryotic kinetochore. Proceedings of the National Academy of Sciences *116*, 12873-12882. 10.1073/pnas.1821945116.
31. Tanaka, T.U., and Zhang, T. (2022). SWAP, SWITCH, and STABILIZE: Mechanisms of Kinetochore–Microtubule Error Correction. Cells *11*, 1462. 10.3390/cells11091462.
32. Jeyaprakash, A.A., Klein, U.R., Lindner, D., Ebert, J., Nigg, E.A., and Conti, E. (2007). Structure of a Survivin–Borealin–INCENP Core Complex Reveals How Chromosomal Passengers Travel Together. Cell *131*, 271-285. 10.1016/j.cell.2007.07.045.

33. Sessa, F., Mapelli, M., Ciferri, C., Tarricone, C., Areces, L.B., Schneider, T.R., Stukenberg, P.T., and Musacchio, A. (2005). Mechanism of Aurora B Activation by INCENP and Inhibition by Hesperadin. Molecular Cell *18*, 379-391. 10.1016/j.molcel.2005.03.031.
34. Hindriksen, S., Lens, S.M.A., and Hadders, M.A. (2017). The Ins and Outs of Aurora B Inner Centromere Localization. Frontiers in Cell and Developmental Biology *5*.
35. Campbell, C.S., and Desai, A. (2013). Tension sensing by Aurora B kinase is independent of survivin-based centromere localization. Nature *497*, 118-121. nature12057 [pii]

10.1038/nature12057.
36. Fischbock-Halwachs, J., Singh, S., Potocnjak, M., Hagemann, G., Solis-Mezarino, V., Woike, S., Ghodgaonkar-Steger, M., Weissmann, F., Gallego, L.D., Rojas, J., et al. (2019). The COMA complex interacts with Cse4 and positions Sli15/Ipl1 at the budding yeast inner kinetochore. Elife *8*. 10.7554/eLife.42879.
37. García-Rodríguez, L.J., Kasciukovic, T., Denninger, V., and Tanaka, T.U. (2019). Aurora B-INCENP Localization at Centromeres/Inner Kinetochores Is Required for Chromosome Bi-orientation in Budding Yeast. Current Biology *29*, 1536-1544.e1534. 10.1016/j.cub.2019.03.051.
38. Hadders, M.A., Hindriksen, S., Truong, M.A., Mhaskar, A.N., Wopken, J.P., Vromans, M.J.M., and Lens, S.M.A. (2020). Untangling the contribution of Haspin and Bub1 to Aurora B function during mitosis. Journal of Cell Biology *219*, e201907087. 10.1083/jcb.201907087.
39. Broad, A.J., DeLuca, K.F., and DeLuca, J.G. (2020). Aurora B kinase is recruited to multiple discrete kinetochore and centromere regions in human cells. Journal of Cell Biology *219*, e201905144. 10.1083/jcb.201905144.
40. Schmitzberger, F., and Harrison, S.C. (2012). RWD domain: a recurring module in kinetochore architecture shown by a Ctf19-Mcm21 complex structure. EMBO Rep *13*, 216-222. embor20121 [pii]

10.1038/embor.2012.1.
41. Biggins, S., and Murray, A.W. (2001). The budding yeast protein kinase Ipl1/Aurora allows the absence of tension to activate the spindle checkpoint. Genes Dev *15*, 3118-3129.
42. Indjeian, V.B., Stern, B.M., and Murray, A.W. (2005). The centromeric protein Sgo1 is required to sense lack of tension on mitotic chromosomes. Science *307*, 130-133. 10.1126/science.1101366.
43. de Regt, A.K., Clark, C.J., Asbury, C.L., and Biggins, S. (2022). Tension can directly suppress Aurora B kinase-triggered release of kinetochore-microtubule attachments. Nature Communications *13*, 2152. 10.1038/s41467-022-29542-8.
44. Akiyoshi, B., Sarangapani, K.K., Powers, A.F., Nelson, C.R., Reichow, S.L., Arellano-Santoyo, H., Gonen, T., Ranish, J.A., Asbury, C.L., and Biggins, S. (2010). Tension directly stabilizes reconstituted kinetochore-microtubule attachments. Nature *468*, 576-579. nature09594 [pii]

10.1038/nature09594.
45. Fenech, E.J., Cohen, N., Kupervaser, M., Gazi, Z., and Schuldiner, M. (2023). A toolbox for systematic discovery of stable and transient protein interactors in baker's yeast. Molecular Systems Biology *19*, e11084. 10.15252/msb.202211084.
46. Gardner, M.K., Bouck, D.C., Paliulis, L.V., Meehl, J.B., O'Toole, E.T., Haase, J., Soubry, A., Joglekar, A.P., Winey, M., Salmon, E.D., et al. (2008). Chromosome congression by Kinesin-5 motor-mediated disassembly of longer kinetochore microtubules. Cell *135*, 894-906. S0092-8674(08)01239-7 [pii]

10.1016/j.cell.2008.09.046.
47. Suzuki, A., Gupta, A., Long, S.K., Evans, R., Badger, B.L., Salmon, E.D., Biggins, S., and Bloom, K. (2018). A Kinesin-5, Cin8, Recruits Protein Phosphatase 1 to Kinetochores and Regulates Chromosome Segregation. Curr Biol *28*, 2697-2704 e2693. 10.1016/j.cub.2018.08.038.

1185 48. Zimniak, T., Fitz, V., Zhou, H., Lampert, F., Opravil, S., Mechtler, K., Stolt-Bergner, P., and
1186 Westermann, S. (2012). Spatiotemporal regulation of Ipl1/Aurora activity by direct Cdk1
1187 phosphorylation. Curr Biol *22*, 787-793. S0960-9822(12)00264-3 [pii]

1188 10.1016/j.cub.2012.03.007.
1189 49. Caldas, G.V., DeLuca, K.F., and DeLuca, J.G. (2013). KNL1 facilitates phosphorylation of outer
1190 kinetochore proteins by promoting Aurora B kinase activity. J Cell Biol *203*, 957-969.
1191 10.1083/jcb.201306054.
1192 50. Desai, A., Rybina, S., Müller-Reichert, T., Shevchenko, A., Shevchenko, A., Hyman, A., and
1193 Oegema, K. (2003). KNL-1 directs assembly of the microtubule-binding interface of the
1194 kinetochore in C. elegans. Genes Dev. *17*, 2421-2435. 10.1101/gad.1126303.
1195 51. Li, S., Garcia-Rodriguez, L.J., and Tanaka, T.U. (2023). Chromosome biorientation requires
1196 Aurora B's spatial separation from its outer kinetochore substrates, but not its turnover at
1197 kinetochores. Current Biology. 10.1016/j.cub.2023.09.006.
1198 52. Liu, D., Vader, G., Vromans, M.J.M., Lampson, M.A., and Lens, S.M.A. (2009). Sensing
1199 Chromosome Bi-Orientation by Spatial Separation of Aurora B Kinase from Kinetochore
1200 Substrates. Science *323*, 1350-1353. 10.1126/science.1167000.
1201 53. Zimniak, T., Stengl, K., Mechtler, K., and Westermann, S. (2009). Phosphoregulation of the
1202 budding yeast EB1 homologue Bim1p by Aurora/Ipl1p. The Journal of Cell Biology *186*, 379-
1203 391. 10.1083/jcb.200901036.
1204 54. Buvelot, S., Tatsutani, S.Y., Vermaak, D., and Biggins, S. (2003). The budding yeast Ipl1/Aurora
1205 protein kinase regulates mitotic spindle disassembly. Journal of Cell Biology *160*, 329-339.
1206 10.1083/jcb.200209018.
1207 55. Kushnirov, V.V. (2000). Rapid and reliable protein extraction from yeast. Yeast *16*, 857-860.
1208 10.1002/1097-0061(20000630)16:9<857::AID-YEA561>3.0.CO;2-B.
1209 56. Katoh, K., Rozewicki, J., and Yamada, K.D. (2019). MAFFT online service: multiple sequence
1210 alignment, interactive sequence choice and visualization. Briefings in Bioinformatics *20*, 1160-
1211 1166. 10.1093/bib/bbx108.
1212 57. Waterhouse, A.M., Procter, J.B., Martin, D.M.A., Clamp, M., and Barton, G.J. (2009). Jalview
1213 Version 2—a multiple sequence alignment editor and analysis workbench. Bioinformatics *25*,
1214 1189-1191. 10.1093/bioinformatics/btp033.
1215 58. Drozdetskiy, A., Cole, C., Procter, J., and Barton, G.J. (2015). JPred4: a protein secondary
1216 structure prediction server. Nucleic Acids Research *43*, W389-W394. 10.1093/nar/gkv332.
1217 59. Mirdita, M., Schütze, K., Moriwaki, Y., Heo, L., Ovchinnikov, S., and Steinegger, M. (2022).
1218 ColabFold: making protein folding accessible to all. Nat. Methods *19*, 679-682.
1219 10.1038/s41592-022-01488-1.
1220 60. Pettersen, E.F., Goddard, T.D., Huang, C.C., Couch, G.S., Greenblatt, D.M., Meng, E.C., and
1221 Ferrin, T.E. (2004). UCSF Chimera--a visualization system for exploratory research and analysis.
1222 Journal of Computational Chemistry *25*, 1605-1612. 10.1002/jcc.20084.
1223 61. Evans, R., O'Neill, M., Pritzel, A., Antropova, N., Senior, A., Green, T., Žídek, A., Bates, R.,
1224 Blackwell, S., Yim, J., et al. (2021). Protein complex prediction with AlphaFold-Multimer.
1225 BioRXiv. https://doi.org/10.1101/2021.10.04.463034.
1226 62. Abramson, J., Adler, J., Dunger, J., Evans, R., Green, T., Pritzel, A., Ronneberger, O., Willmore, L.,
1227 Ballard, A.J., Bambrick, J., et al. (2024). Accurate structure prediction of biomolecular
1228 interactions with AlphaFold 3. Nature *630*, 493-500. 10.1038/s41586-024-07487-w.
1229 63. Jumper, J., Evans, R., Pritzel, A., Green, T., Figurnov, M., Ronneberger, O., Tunyasuvunakool, K.,
1230 Bates, R., Žídek, A., Potapenko, A., et al. (2021). Highly accurate protein structure prediction
1231 with AlphaFold. Nature *596*, 583-589. 10.1038/s41586-021-03819-2.
1232 64. Emsley, P., and Cowtan, K. (2004). Coot: model-building tools for molecular graphics. Acta
1233 Crystallogr D Biol Crystallogr *60*, 2126-2132. 10.1107/S0907444904019158.
1234 65. Krissinel, E., and Henrick, K. (2007). Inference of macromolecular assemblies from crystalline
1235 state. J Mol Biol *372*, 774-797. S0022-2836(07)00642-0 [pii]

10.1016/j.jmb.2007.05.022.

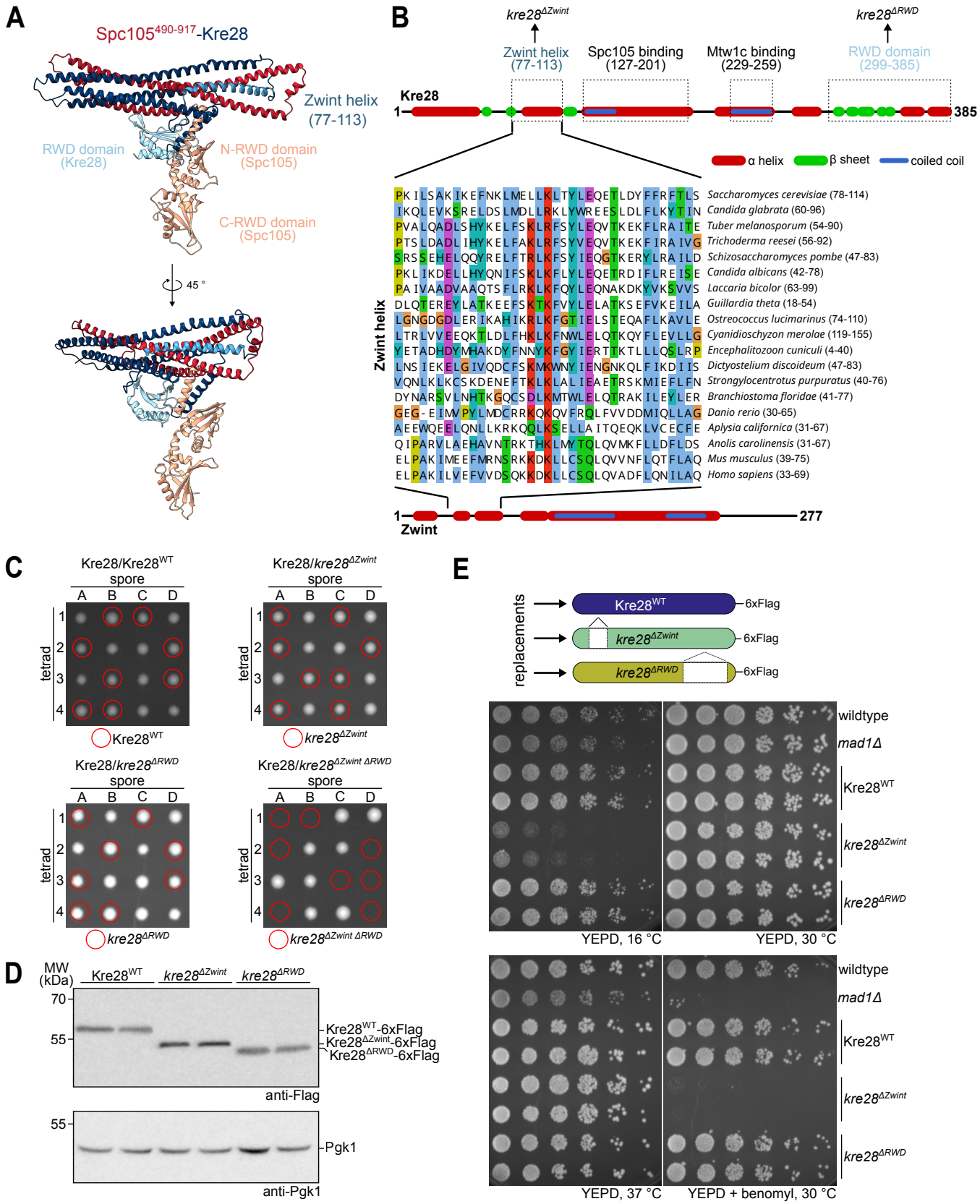
A
Spc105490-917-Kre28
Zwint helix (77-113)
RWD domain (Kre28)
N-RWD domain (Spc105)
C-RWD domain (Spc105)
45 °
B
kre28ΔZwint
kre28ΔRWD
Zwint helix (77-113)
Spc105 binding (127-201)
Mtw1c binding (229-259)
RWD domain (299-385)
Kre28
1
385
α helix
β sheet
coiled coil
Zwint helix
Saccharomyces cerevisiae (78-114)
Candida glabrata (60-96)
Tuber melanosporum (54-90)
Trichoderma reesei (56-92)
Schizosaccharomyces pombe (47-83)
Candida albicans (42-78)
Laccaria bicolor (63-99)
Guillardia theta (18-54)
Ostreococcus lucimarinus (74-110)
Cyanidioschyzon merolae (119-155)
Encephalitozoon cuniculi (4-40)
Dictyostelium discoideum (47-83)
Strongylocentrotus purpuratus (40-76)
Branchiostoma floridae (41-77)
Danio rerio (30-65)
Aplysia californica (31-67)
Anolis carolinensis (31-67)
Mus musculus (39-75)
Homo sapiens (33-69)
1
Zwint
277
C
Kre28/Kre28WT
Kre28/kre28ΔZwint
Kre28/kre28ΔRWD
Kre28/kre28ΔZwint ΔRWD
spore
A B C D
tetrad
1 2 3 4
Kre28WT
kre28ΔZwint
kre28ΔRWD
kre28ΔZwint ΔRWD
D
MW (kDa)
Kre28WT
kre28ΔZwint
kre28ΔRWD
70
55
Kre28WT-6xFlag
Kre28ΔZwint-6xFlag
Kre28ΔRWD-6xFlag
anti-Flag
55
Pgk1
anti-Pgk1
E
replacements
Kre28WT
kre28ΔZwint
kre28ΔRWD
6xFlag
wildtype
mad1Δ
Kre28WT
kre28ΔZwint
kre28ΔRWD
YEPD, 16 °C
YEPD, 30 °C
YEPD, 37 °C
YEPD + benomyl, 30 °C

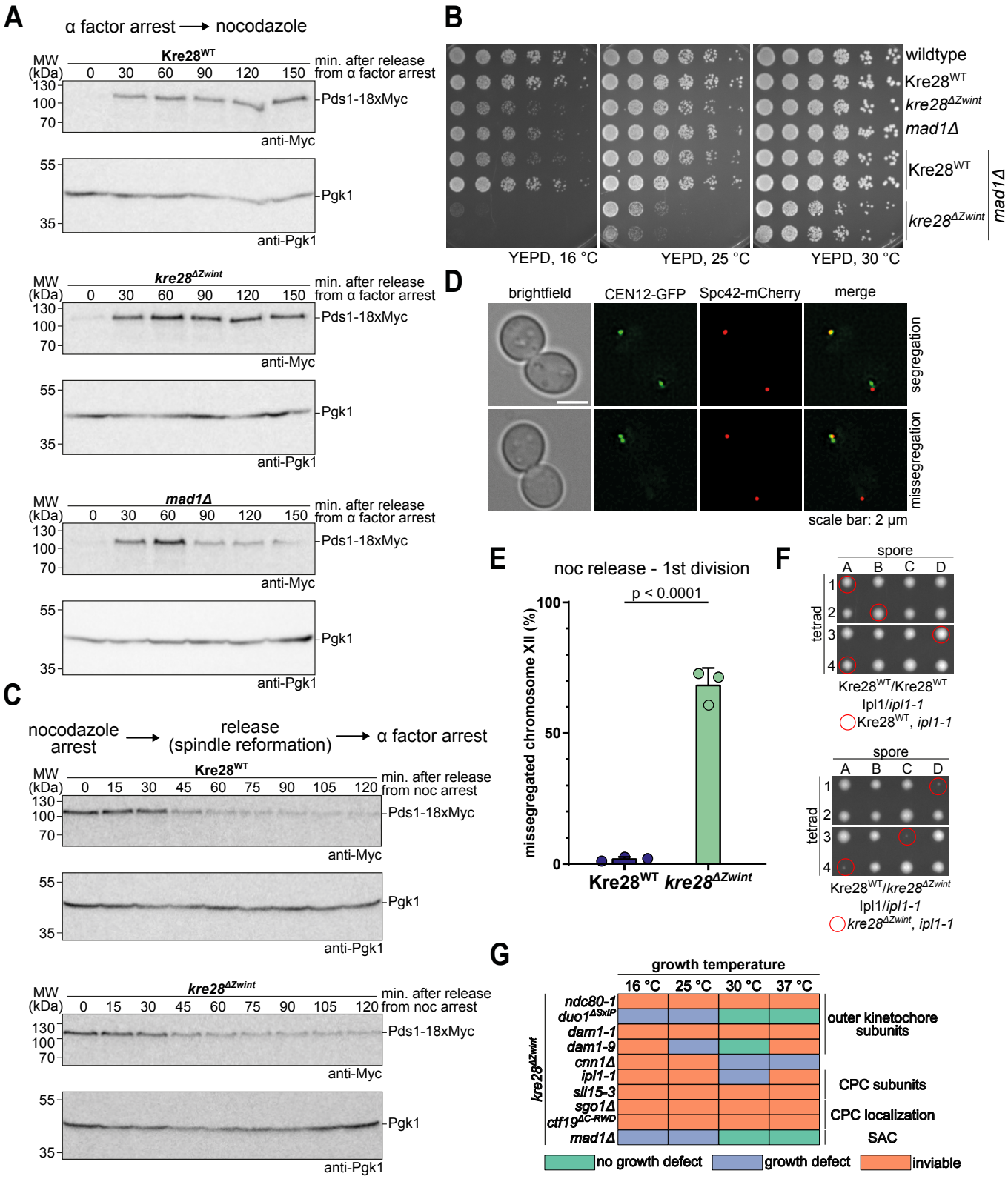
A
α factor arrest → nocodazole
Kre28WT
kre28ΔZwint
mad1Δ
MW (kDa)
min. after release from α factor arrest
0 30 60 90 120 150
130
100
70
55
35
Pds1-18xMyc
anti-Myc
Pgk1
anti-Pgk1
B
wildtype
Kre28WT
kre28ΔZwint
mad1Δ
YEPD, 16 °C
YEPD, 25 °C
YEPD, 30 °C
C
nocodazole arrest → release (spindle reformation) → α factor arrest
0 15 30 45 60 75 90 105 120
min. after release from noc arrest
D
brightfield
CEN12-GFP
Spc42-mCherry
merge
segregation
missegregation
scale bar: 2 µm
E
noc release - 1st division
p < 0.0001
missegregated chromosome XII (%)
100
50
0
Kre28WT
kre28ΔZwint
F
spore
A B C D
tetrad
1 2 3 4
Kre28WT/Kre28WT
Ipl1/ipl1-1
Kre28WT, ipl1-1
Kre28WT/kre28ΔZwint
kre28ΔZwint, ipl1-1
G
growth temperature
16 °C 25 °C 30 °C 37 °C
ndc80-1
duo1ΔSxIP
dam1-1
dam1-9
cnn1Δ
ipl1-1
sli15-3
sgo1Δ
ctf19ΔC-RWD
mad1Δ
kre28ΔZwint
outer kinetochore subunits
CPC subunits
CPC localization
SAC
no growth defect
growth defect
inviable

Figure 3 **Dudziak et al., 2024**

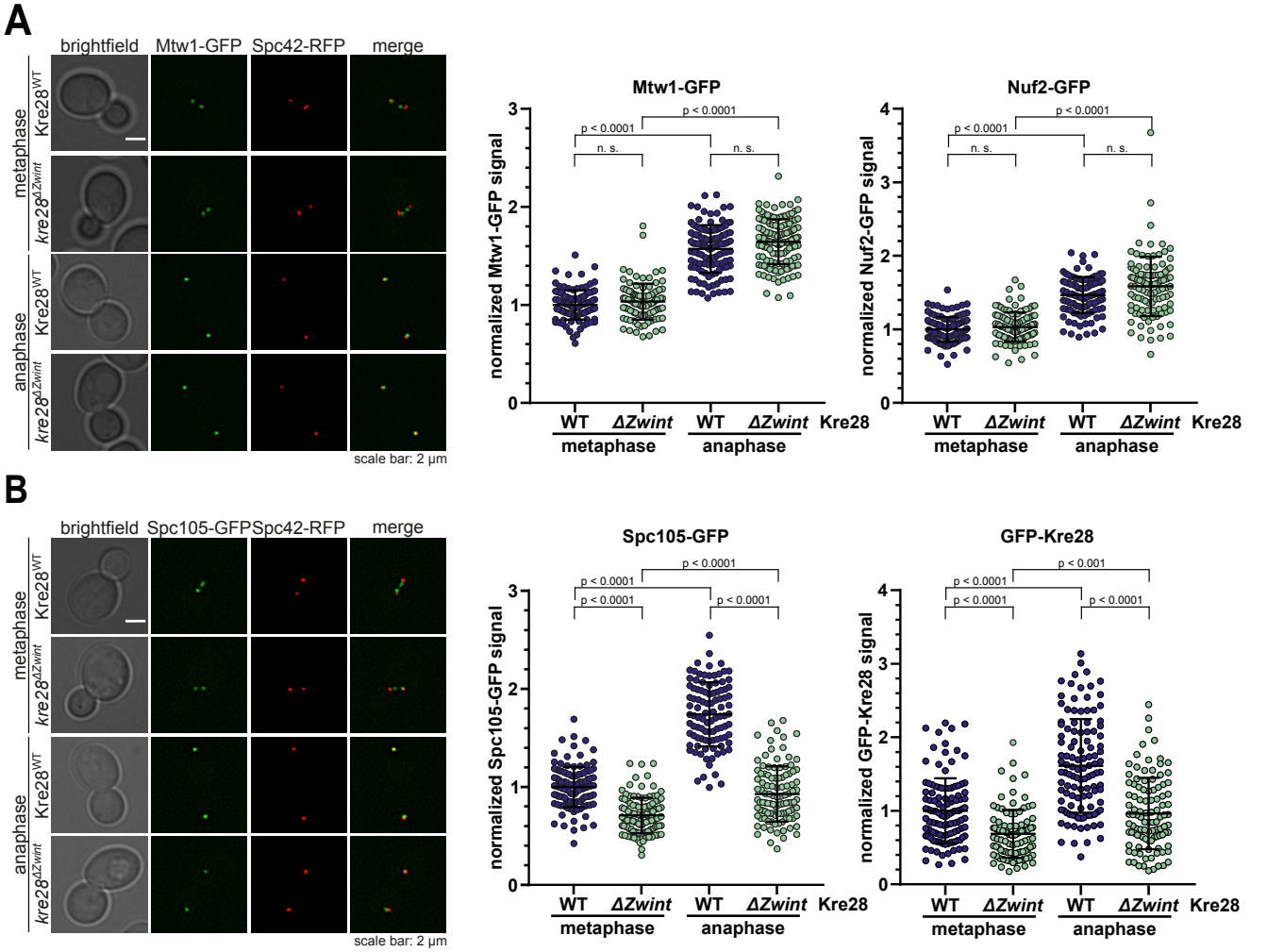

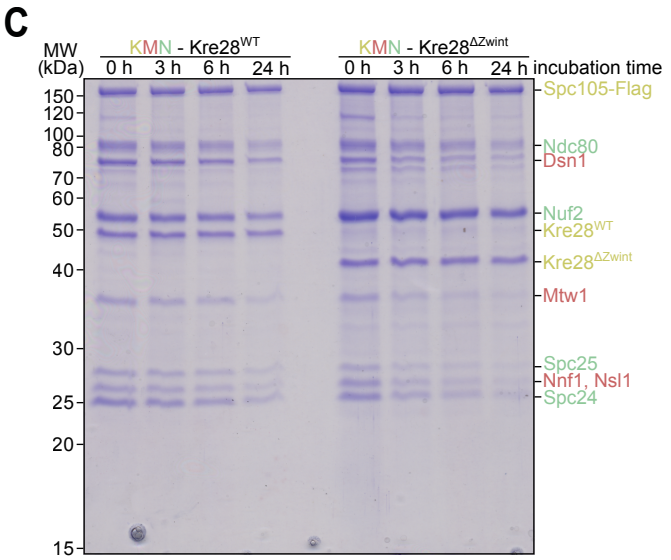

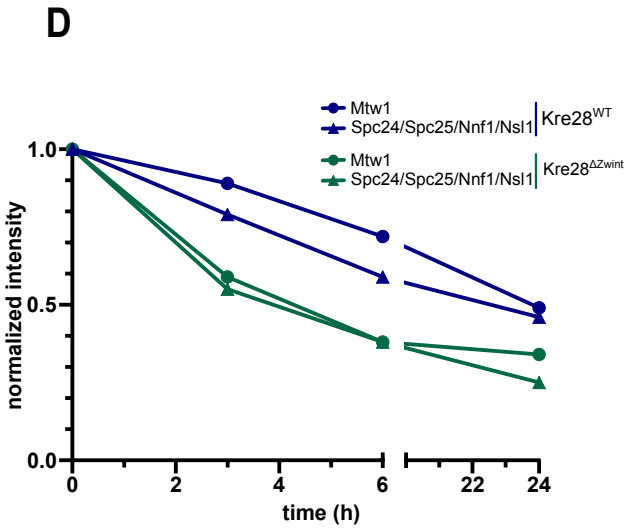

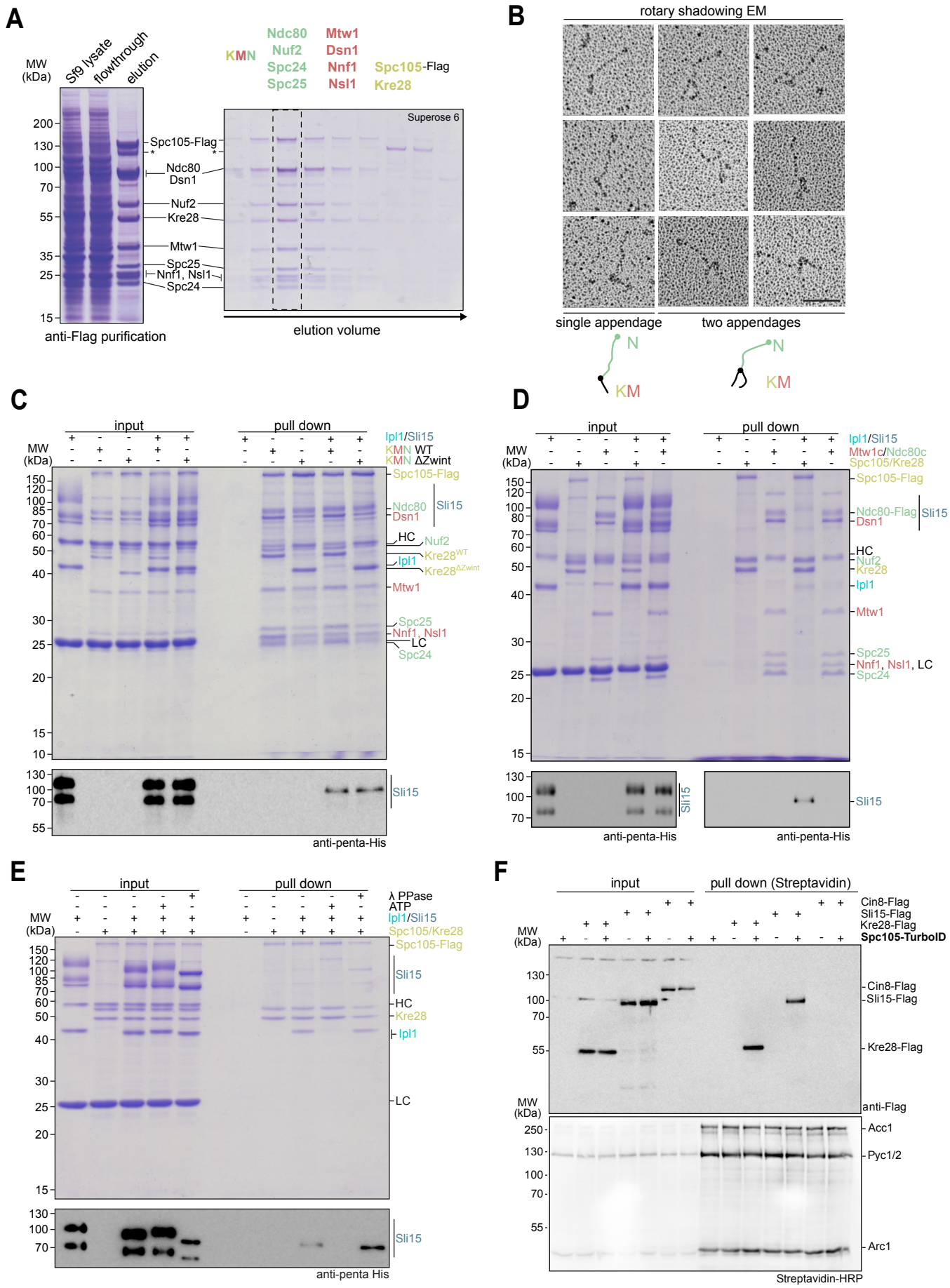
A
MW (kDa)
Sf9 lysate
flowthrough
elution
KMN
Ndc80
Nuf2
Spc24
Spc25
Mtw1
Dsn1
Nnf1
Nsl1
Spc105-Flag
Kre28
Superose 6
Spc105-Flag
Ndc80
Dsn1
Nuf2
Kre28
Mtw1
Spc25
Nnf1, Nsl1
Spc24
anti-Flag purification
elution volume
B
rotary shadowing EM
single appendage
two appendages
N
KM
C
input
pull down
Ipl1/Sli15
KMN WT
KMN ΔZwint
Spc105-Flag
Sli15
Ndc80
Dsn1
HC
Nuf2
Kre28WT
Ipl1
Kre28ΔZwint
Mtw1
Spc25
Nnf1, Nsl1
LC
Spc24
anti-penta-His
D
Mtw1c/Ndc80c
Spc105/Kre28
Ndc80-Flag
anti-penta-His
E
λ PPase
ATP
anti-penta His
F
input
pull down (Streptavidin)
Cin8-Flag
Sli15-Flag
Kre28-Flag
Spc105-TurboID
anti-Flag
Acc1
Pyc1/2
Arc1
Streptavidin-HRP

Figure 5 **Dudziak et al., 2024**

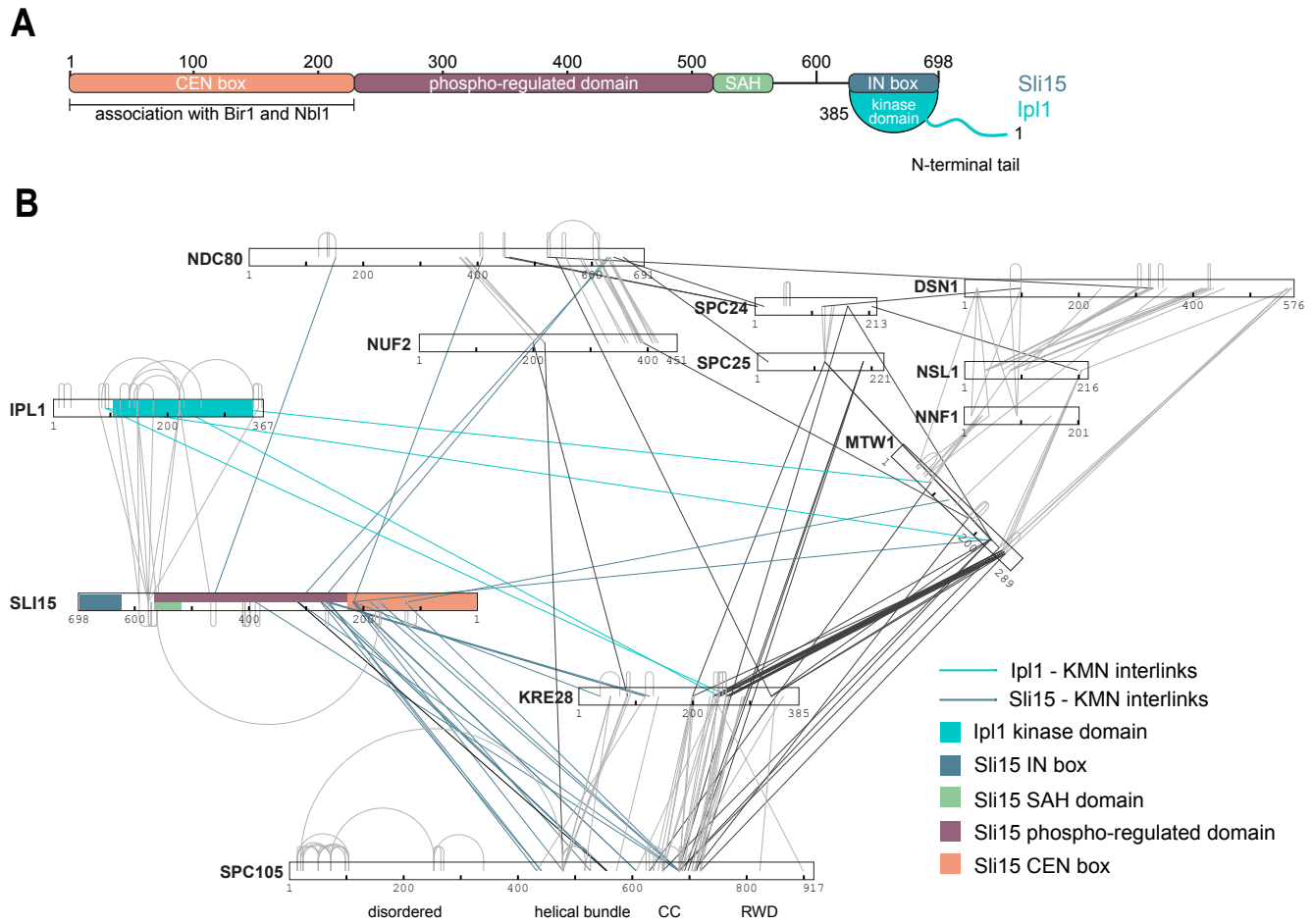

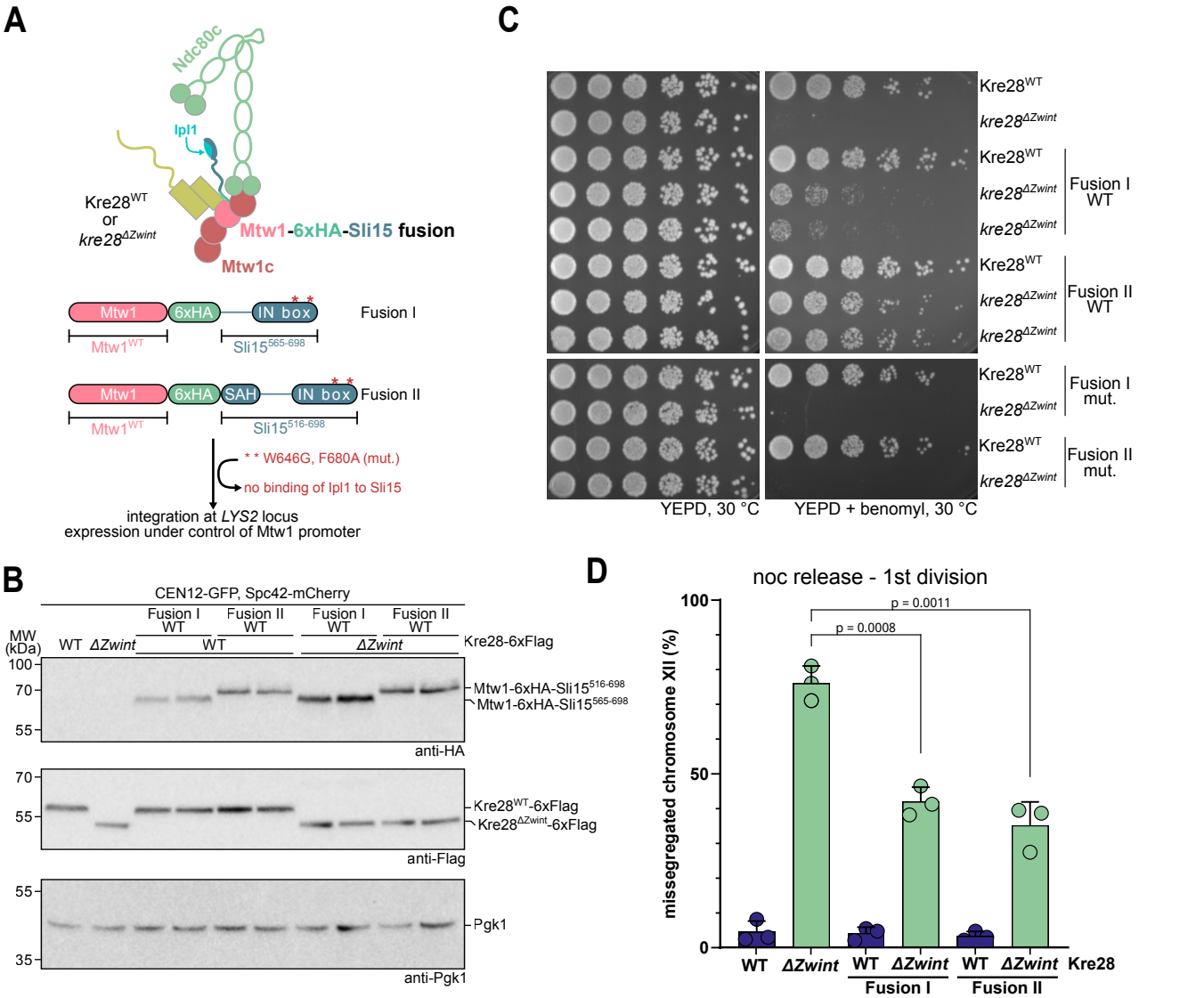
A
Ndc80c
Ipl1
Kre28WT or kre28ΔZwint
Mtw1-6xHA-Sli15 fusion
Mtw1c
Mtw1
6xHA
IN box
Fusion I
Mtw1WT
Sli15565-698
SAH
Fusion II
Sli15516-698
* * W646G, F680A (mut.)
no binding of Ipl1 to Sli15
integration at LYS2 locus
expression under control of Mtw1 promoter
B
CEN12-GFP, Spc42-mCherry
MW (kDa)
WT ΔZwint
Fusion I WT
Fusion II WT
Kre28-6xFlag
Mtw1-6xHA-Sli15516-698
Mtw1-6xHA-Sli15565-698
anti-HA
Kre28WT-6xFlag
Kre28ΔZwint-6xFlag
anti-Flag
Pgk1
anti-Pgk1
C
Kre28WT
kre28ΔZwint
Fusion I WT
Fusion II WT
Fusion I mut.
Fusion II mut.
YEPD, 30 °C
YEPD + benomyl, 30 °C
D
noc release - 1st division
missegregated chromosome XII (%)
p = 0.0011
p = 0.0008
WT
ΔZwint
Fusion I
Fusion II
Kre28

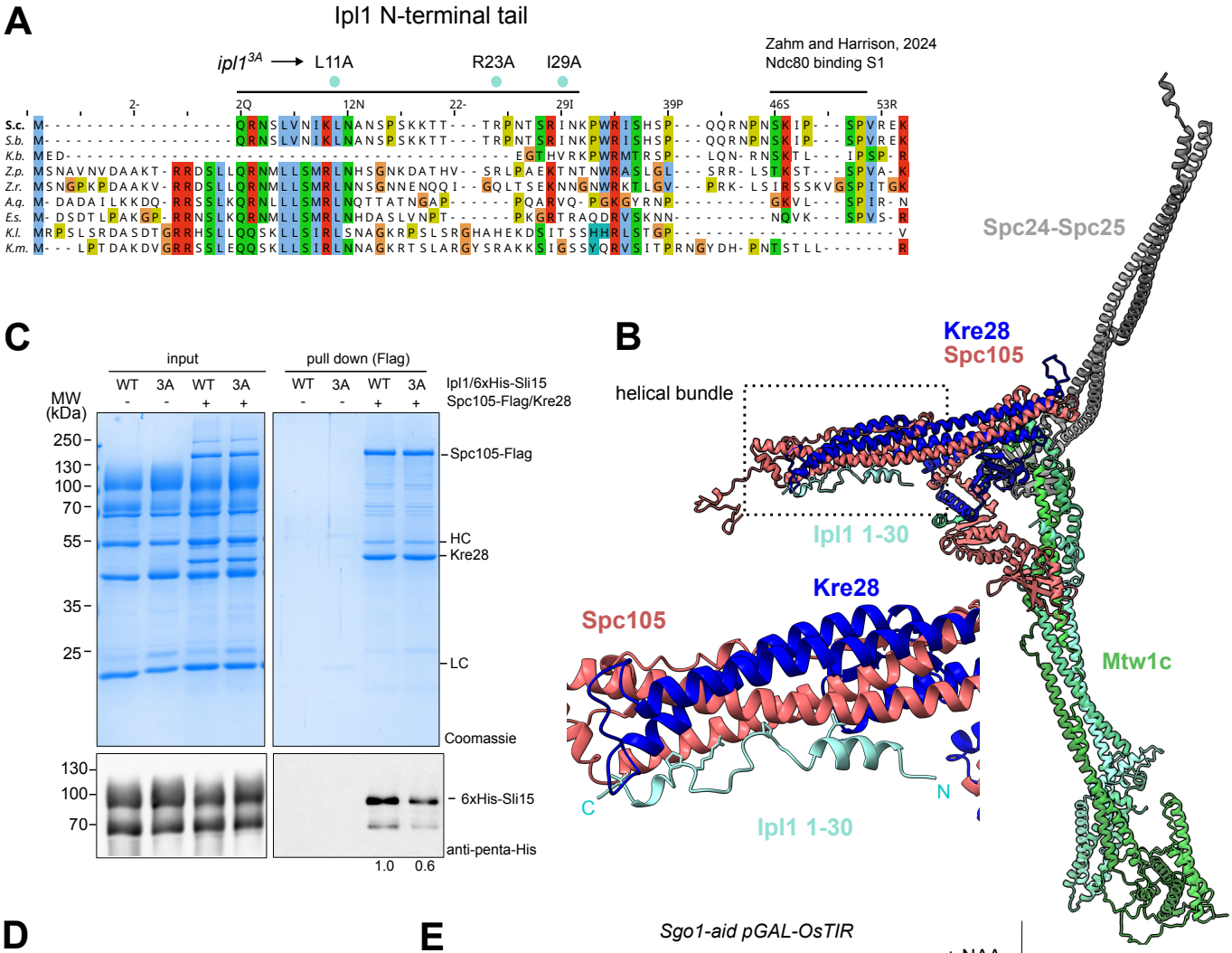
A
Ipl1 N-terminal tail
ipl1^3A → L11A
R23A
I29A
Zahm and Harrison, 2024
Ndc80 binding S1
S.c.
S.b.
K.b.
Z.p.
Z.r.
A.q.
E.s.
K.l.
K.m.
B
helical bundle
Kre28
Spc105
Ipl1 1-30
Spc24-Spc25
Mtw1c
C
input
pull down (Flag)
WT 3A WT 3A
WT 3A WT 3A
Ipl1/6xHis-Sli15
Spc105-Flag/Kre28
MW (kDa)
250
130
100
70
55
35
25
Spc105-Flag
HC
Kre28
LC
Coomassie
6xHis-Sli15
anti-penta-His
1.0 0.6
D
Sli15
CEN box
IN box
kinase
C
N
sgo1-aid
ctf19ΔRWD-C
ipl1^3A
ipl1Δ2-30
ipl1Δ2-55
centromere/inner KT recruitment pathways
outer KT binding motifs
E
Sgo1-aid pGAL-OsTIR
+ NAA
ipl1^WT
ipl1^3A
ipl1Δ2-30
ipl1Δ2-55
YEPD, 30 °C
YEP Raff/Gal, 30 °C
F
CTF19
ctf19ΔRWD-C
ipl1^WT
ipl1^3A
ipl1Δ2-30
ipl1Δ2-55
YEPD, 30 °C
G
CTF19
ctf19ΔRWD-C
ipl1^WT
ipl1^3A
ipl1Δ2-30
ipl1Δ2-55
YEPD + benomyl, 30 °C

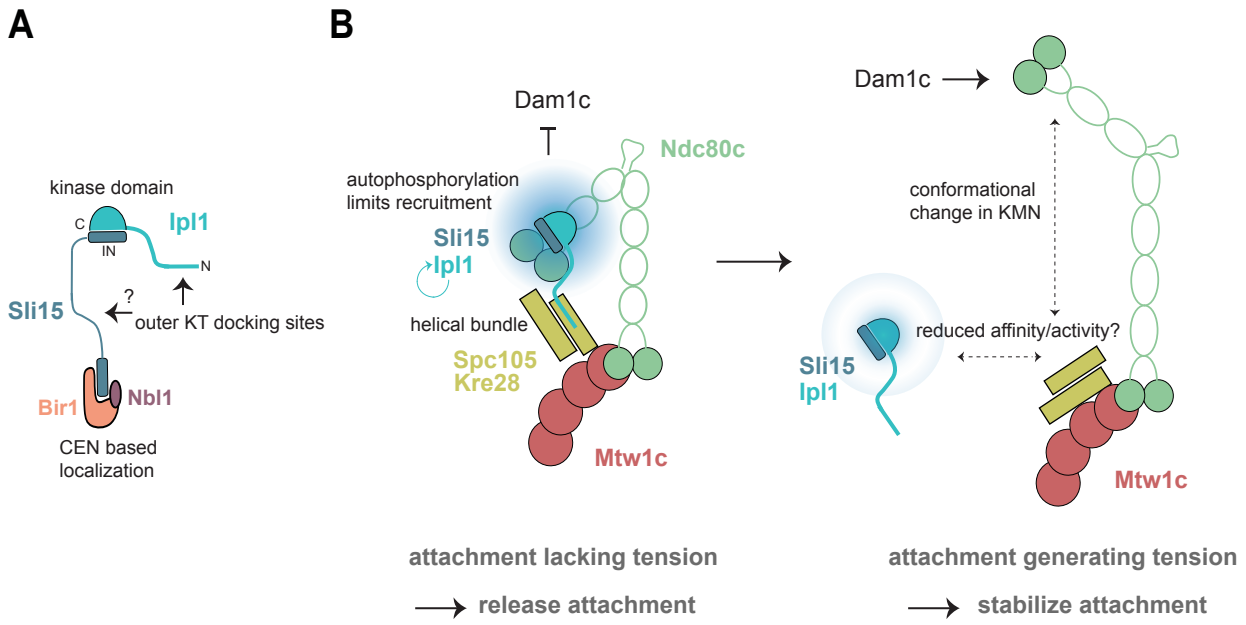
A
kinase domain
C
IN
Ipl1
N
Sli15
?
outer KT docking sites
Bir1
Nbl1
CEN based
localization
B
Dam1c
Ndc80c
autophosphorylation
limits recruitment
Sli15
Ipl1
helical bundle
Spc105
Kre28
Mtw1c
Dam1c
conformational
change in KMN
reduced affinity/activity?
Sli15
Ipl1
Mtw1c
attachment lacking tension
release attachment
attachment generating tension
stabilize attachment